frontiers | Frontiers in Earth Science

TYPE Original Research
PUBLISHED 10 November 2022
DOI 10.3389/feart.2022.1009715

OPEN ACCESS

EDITED BY
Liang Zhang,
China University of Geosciences, China

REVIEWED BY
Linnan Guo,
Chengdu Geological Survey Center, China
Peng Chai,
Chinese Academy of Geological Sciences (CAGS), China
Ruihong Li,
Chinese Academy of Geological Sciences (CAGS), China

*CORRESPONDENCE
Naijie Chi,
chinaijie@163.com
Zuozhen Han,
Hanzz@163.com

SPECIALTY SECTION
This article was submitted to Geochemistry, a section of the journal *Frontiers in Earth Science*

RECEIVED 02 August 2022
ACCEPTED 20 October 2022
PUBLISHED 10 November 2022

CITATION
Chi N, Han Z, Liu C, Zhang W, Zhang Y, Shan W, Li Z, Li M, Wang X and Sun Y (2022), Metallogenic mechanism of the Houge'zhuang gold deposit, Jiaodong, China: Evidence from fluid inclusion, *in situ* trace element, and sulfur isotope compositions.
Front. Earth Sci. 10:1009715.
doi: 10.3389/feart.2022.1009715

Metallogenic mechanism of the Houge'zhuang gold deposit, Jiaodong, China: Evidence from fluid inclusion, *in situ* trace element, and sulfur isotope compositions

Naijie Chi[1,2]*, Zuozhen Han[1]*, Chuan'e Liu[3], Wei Zhang[2], Yanhui Zhang[4], Wei Shan[2], Zengsheng Li[2], Min Li[2], Xiufeng Wang[2] and Yuqin Sun[2]

[1]College of Earth Science and Engineering, Shandong University of Science and Technology, Qingdao, China, [2]Key Laboratory of Gold Mineralization Processes and Resource Utilization, MNR Shandong Provincial Key Laboratory of Metallogenic Geological Process and Resource Utilization, Shandong Institute of Geological Sciences, Jinan, China, [3]Shandong Provincial Geo-mineral Engineering Exploration Institute, Jinan, China, [4]Shandong Institute of Geophysical and Geochemical Exploration, Jinan, China

The Houge'zhuang gold deposit, located in the Penglai–Qixia gold belt of the Jiaodong peninsula, is a representative auriferous quartz vein-style deposit. Pyrite is the most common and main gold-bearing mineral and shows complex textures in the Houge'zhuang gold deposit. Study of ore-related pyrite is of great significance for understanding the metallogenesis of this deposit, especially the gold precipitation mechanism. The present study applied systematic microscopic observation, fluid inclusion analysis, electron microprobes**,** *in situ* LA-ICP-MS trace-element analysis, and *in situ* sulfur isotope analyses. Three types of fluid inclusions were identified, among which the ore-forming fluids exhibited medium–low salinity and temperature, with the fluid inclusions mainly comprising H_2O and CO_2. Three types of pyrites were identified: 1) Py0, characterized by low concentrations of As and Au and low $\delta^{34}S$ values (5.51–6.86‰). 2) Py1, found in the gold-quartz-pyrite veins and homogeneous in chemical composition with no obvious zonal growth but with notably more gold and chalcopyrite inclusions. Py1 contained medium and uniform concentrations of As and was Au-rich, with $\delta^{34}S$ values ranging from 7.13 to 7.89‰ (mean 7.44‰). 3) Py2 contained arsenic-bearing pyrite and was found in quartz-polymetallic sulfide veins, with distinct As enrichment and As-rich rims of pyrite and growth zoning. Consequently, the primary ore-forming fluids passed through some arsenic and $\delta^{34}S$-rich sedimentary rocks, such as the Jingshan, Fenzishan, and Penglai groups. With the occurrence of stable water-rock interaction, the extracted fluids were enriched for As and $\delta^{34}S$. Furthermore, Au was closely associated with As, visible gold grains tended to occur in association with Py1 at stage II, and invisible gold was related to the Au-As-rich Py2 of stage III. The As-

bearing pyrites shared a close spatiotemporal relationship with gold, playing an important role in the formation and exploration of high-grade gold deposits.

KEYWORDS

Houge'zhuang gold deposit, ore-related pyrite, *in situ* trace element, lattice gold, *in situ* sulfur isotope

Introduction

The Jiaodong Peninsula is the largest and most productive gold province in China, with more than 5000 t of gold reserves. Although the Jiaodong area accounts for only 0.2% of the total area of the country, it holds about 25% of China's total gold reserves (Deng et al., 2006; Liu et al., 2014; Yang et al., 2016a; Fan et al., 2016; Yang et al., 2018; Chai et al., 2020a; Deng et al., 2020a; Deng et al., 2020b; Deng et al., 2020c; Zhang et al., 2020; Wang et al., 2021). In this region, pyrite is the most common and important metal sulfide mineral widely distributed within the gold orebodies and country rocks. The content of pyrite in gold ores directly affects the gold grade. Statistics of the main gold deposit types in the Jiaodong area indicate that pyrite accounts for more than 90% of the total metal minerals. More than 85% of the gold is distributed in the pyrite interstice and fissures, and within pyrite crystals (Li et al., 2007), with the remainder being invisible gold, primarily nanogold and lattice gold (Li J. et al., 2020). The nanogold is adsorbed by pyrite (Möller and Kersten, 1994; Simon et al., 1999a; Simon et al., 1999b; Li R. H. et al., 2020), while lattice Au is likely present as Au^{+} or Au^{3+} in the lattice of arsenic-bearing pyrite (Arehart et al., 1993; Chouinard et al., 2005; Reich et al., 2005; Deditius et al., 2014; Meng et al., 2022). Au is closely associated with As, such as As^{1-} + Au^{1+} sitting at the atom sites of S^{2-} + Fe^{2-} or As^{3+}+Au^{1+} replacing Fe^{2+}. The element changes in pyrite can appear in the micro-texture of pyrite. Consequently, the micro-composition and trace elements of pyrite can record the transportation and deposition of gold; thus, detailed studies on gold-bearing pyrite are crucial to elucidate the genesis and prospecting of gold deposits in this area (Barker et al., 2009; Large et al., 2009; Cook et al., 2009; Cook et al., 2013; Tanner et al., 2016; Yang et al., 2016a; Chai et al., 2019a,b,Chai et al., 2019c).

Previous studies on the gold deposits in the Jiaodong area have primarily focused on the petrology, geochronology, elemental and isotopic geochemistry, and structure, among others; however, the factors controlling the high-grade gold mineralization and the origin and relevant implication for transportation and deposition of gold remain controversial (Hou et al., 2006; Hou et al., 2007a; Goldfarb and Santosh, 2014; Yan et al., 2014; Li et al., 2015; Song et al., 2015; Zhu et al., 2015; Deng et al., 2017; Deng et al., 2018).

The Penglai–Qixia belt is an important gold belt in the Jiaodong Peninsula, which contains several medium-sized gold deposits. These deposits are notable for the local presence of native gold shoots, which are rarely seen in the other regions of the Jiaodong Peninsula. Several high-grade gold ores in many orogenic Au deposits are also present (Ma et al., 2015; Feng, et al., 2018; Feng, et al., 2020). They are commonly associated with As-rich pyrite and/or arsenopyrite. However, pyrites from the Jiaodong gold deposits generally contain negligible As, while arsenopyrite is rare, which restricts research on the relationship between Au and As in Jiaodong. However, arsenic-bearing pyrite (As up to 2.5wt%) and abundant visible gold grains have recently been reported in the Houge'zhuang gold deposit in the Penglai–Qixia belt, indicating a close spatial association with visible Au. This finding provides an opportunity to study the behaviors of Au and As during gold mineralization and to better understand the origin of high-grade ores in this deposit.

Advances in microanalytical techniques such as EMPA and LA-ICP-MS have allowed the observation of detailed elemental and isotopic information from individual pyrites with complex internal micro-textures. These details can help in unraveling the growth histories and deducing the sources, nature, and evolution of relevant ore-forming fluids.

Based on previous research, the present study systematically assessed gold-bearing pyrites from the Houge'zhuang deposit by conducting detailed field geological investigation, sampling, microscope observation, major and trace element mapping, and *in situ* trace element and sulfur isotopic analyses. These data may facilitate the better elucidation of the behaviors of As and Au during the gold mineralization process and provide a thorough understanding of the mechanism of gold mineralization and precipitation in the Houge'zhuang deposit.

Regional geology

The Jiaodong peninsula is an important gold-enriched area in China. Tectonically, this area is located in the Jiaobei uplift of the Jiaoliao uplift on the eastern margin of the North China Plate (Figure 1) (Zhai and Santosh, 2011; Yang et al., 2016a; Yang et al., 2016b; Deng and Wang, 2016). The basement rocks in the Jiaodong Peninsula include the Jiaodong Group of the Archean TTG rock series, the Jingshan and the Fenzishan Groups of lower Proterozoic metamorphic rocks, and the Penglai Group of upper Proterozoic metamorphic rocks (Wang et al., 2011). In upward sequence order, the clastic and carbonate rocks of the Penglai Group overlie the lower Proterozoic Jingshan and Fenzishan groups. The Linyi Formation of quaternary loose sediments is distributed along the seashore and riverside on the north of the study area.

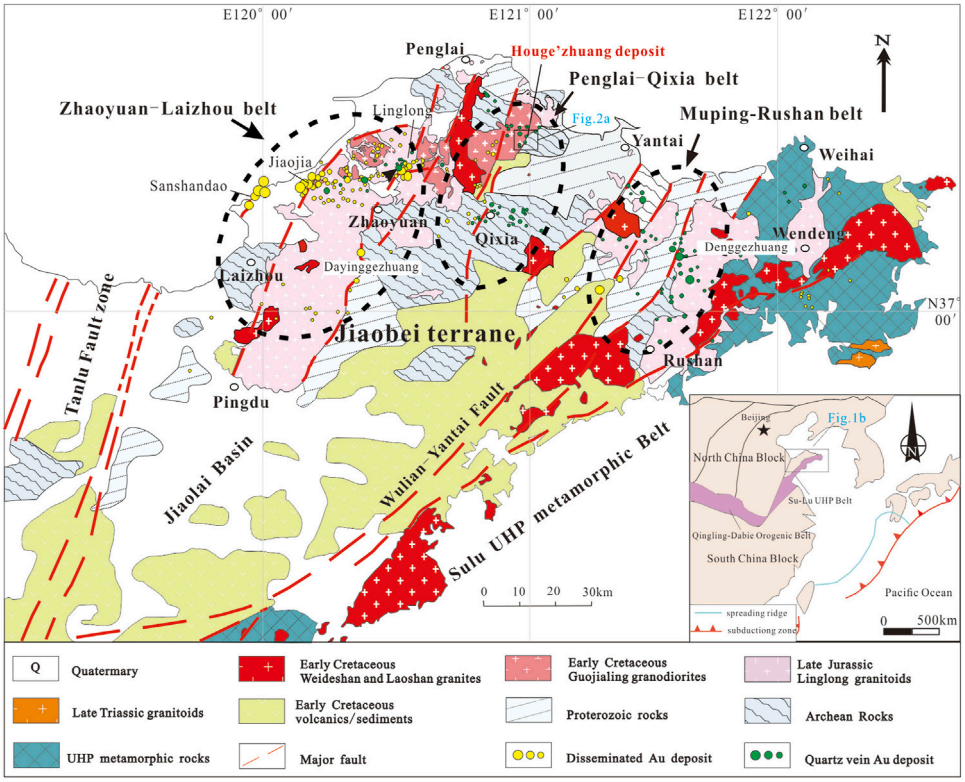

FIGURE 1
Geological map of the Jiaodong gold province showing the major gold deposits and lithological units. Modified after Wen et al. (2015).

Mesozoic granitoid, which covers more than two-thirds of the bedrock outcrops in this area, consists primarily of Linglong granite, aged 160–150 Ma(Yang et al., 2014; Deng et al., 2015a; Deng et al., 2015b; Yang et al., 2018a; Yang et al., 2018b; Yang et al., 2020), and Guojialing porphyritic granodiorite, aged 132–126 Ma, which contains most of the gold deposits in the area. Dyke rocks such as lamprophyre, diorite porphyrite, and diabase are also present in the study area.

The Jiaodong gold belt is divided into the Zhaoyuan–Laizhou, Penglai–Qixia, and Muping–Rushan belts. The Houge'zhuang deposit, the study area, is located in the Penglai–Qixia belt, which is characterized by many medium to large-sized quartz vein-style gold deposits controlled by the NE and NNE-trending Qixia, Xiaogu'jia faults (Feng et al., 2018; Feng et al., 2020).

Deposit geology

Geology of the Houge'zhuang deposit

The Houge'zhuang gold deposit is a medium-sized and representative auriferous quartz vein-style deposit controlled by the Daliu'hang fault, with a strike generally in the NNE direction (15°–30°) and dip to the SE, with steep dipping angles (60–65°) and lengths ranging from hundreds to thousands of meters but widths of only a few meters (Figure 2A).

In the gold field, the widely distributed magmatic rocks are Early Cretaceous Guojialing granodiorite, which is the main host for the Au-bearing quartz veins (Hou et al., 2004; Yan et al., 2014). The gold deposit is surrounded by basic-intermediate to felsic dikes, such as lamprophyre, diorite porphyrite, and granite porphyry, among others. The terrane is composed of the Proterozoic Jinshan Group, Early Cretaceous Qingshan Group, and Quaternary formation. Precambrian metamorphic basement and Cretaceous sedimentary are present in the southern part of this deposit.

The Houge'zhuang gold deposit is mainly composed of three gold veins, which occur mainly in the form of veinlets, reticulate veins, and agglomerates that strike generally in the NNE direction (5–20°) and dip to the NW, with steep dipping angles (60–75°), showing the characteristics of pinch-out and recurrence (Figures 2B, 3A). The gold grade varies from 0.3 to 52.4 g/t, with an average of 7.95 g/t. The ore is dominated by a massive and disseminated structure.

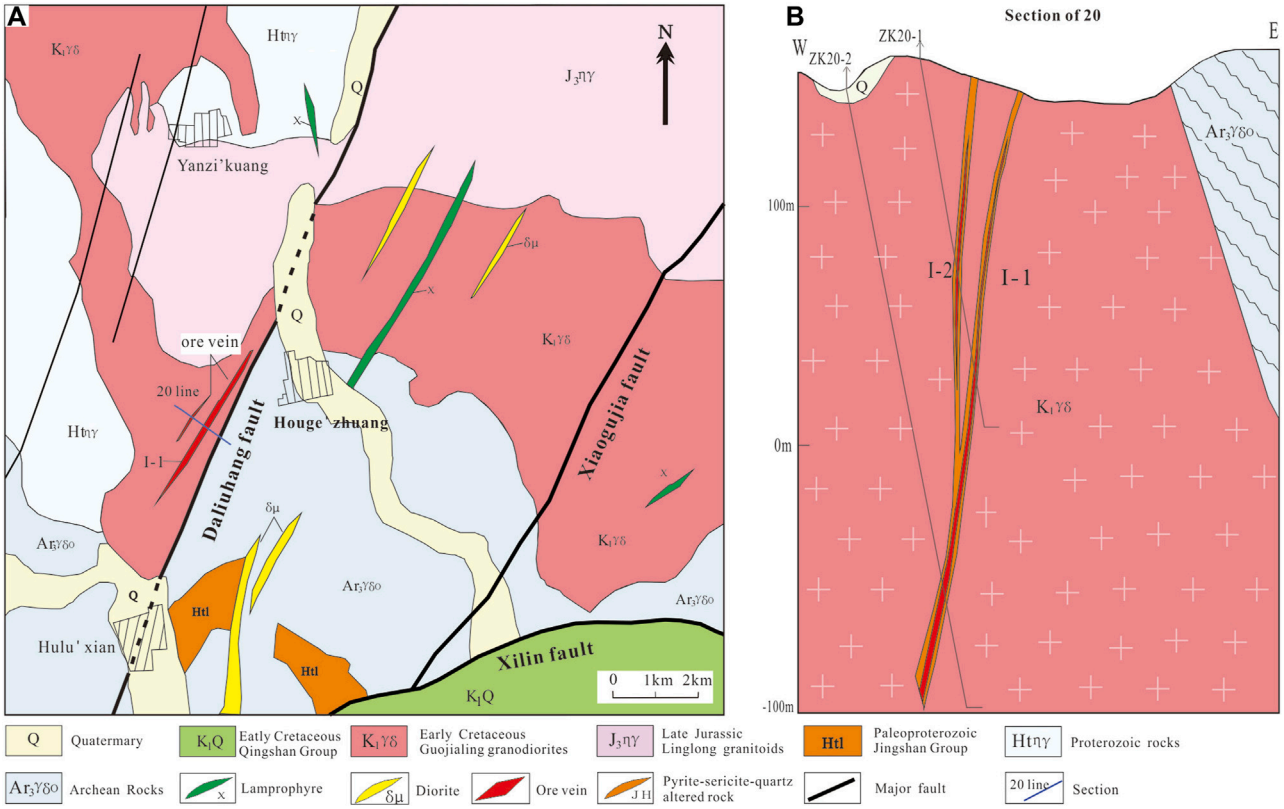

FIGURE 2
Geological map of the Houge'zhuang gold mining area **(A)** and the geological section of Line 20 **(B)**.

Mineral assemblage and paragenetic sequence

The ore minerals of the Houge'zhuang deposit include pyrite, sphalerite, galena, and other sulfides. The subordinate minerals are K-feldspar, carbonates, chlorite, kaolinite, chalcopyrite, and electrum. Tellurobismuthite occurs locally, with trace amounts of arsenopyrite, pyrrhotite, enargite, hessite, and tetrahedrite (Figure 4). Pyrite, sphalerite, galena, and other sulfides account for 10–60% of the total minerals; among them, pyrite is the most closely related to gold mineralization and is the most important gold-bearing mineral (Figure 5). The alteration halos are typically 0.2–1 m wide, are weakly developed, and include potassic alteration, silicification, sericitization, and sericite-quartz-pyrite alterations.

Based on the detailed microscopic observations and their cross-cutting relationships, four principal stages similar to the other Jiaodong gold deposits can be distinguished, namely, the pyrite-quartz (I), gold-quartz-pyrite (II), gold polymetallic sulfides (III), and quartz-carbonate (IV) stages, wherein stages II and III are the main gold mineralization stages. Stage I, which is the early stage of mineralization, mainly comprises milk-barren quartz, with minor sericite and fine pyrite as inclusions (Figure 4A). Very little or no gold mineralization occurs at this stage (Figure 3A). Stage II is defined by quartz-pyrite veins, which commonly cut stage I quartz veins (Figures 3B–D). In this stage, the predominant mineral is pyrite, with small amounts of quartz and chalcopyrite. Gold mainly occurs in the form of inclusion, interstitial, and fissure gold, which are commonly present in pyrite and quartz grains, as well as occasionally along the boundaries between pyrite grains. Stage III is characterized by gold-quartz-polymetallic sulfide veins dominated by pyrite, arsenopyrite, chalcopyrite, galena, sphalerite, and arsenic. The gold is primarily invisible gold, with the presence of nano-gold and crystal-gold. Stage IV is characterized by barren quartz–calcite veins, with almost no gold mineralization.

Sampling and analytical methods

Sampling and sample preparation

Representative samples were collected from the underground workings of the Houge'zhuang deposit. The samples were cut and

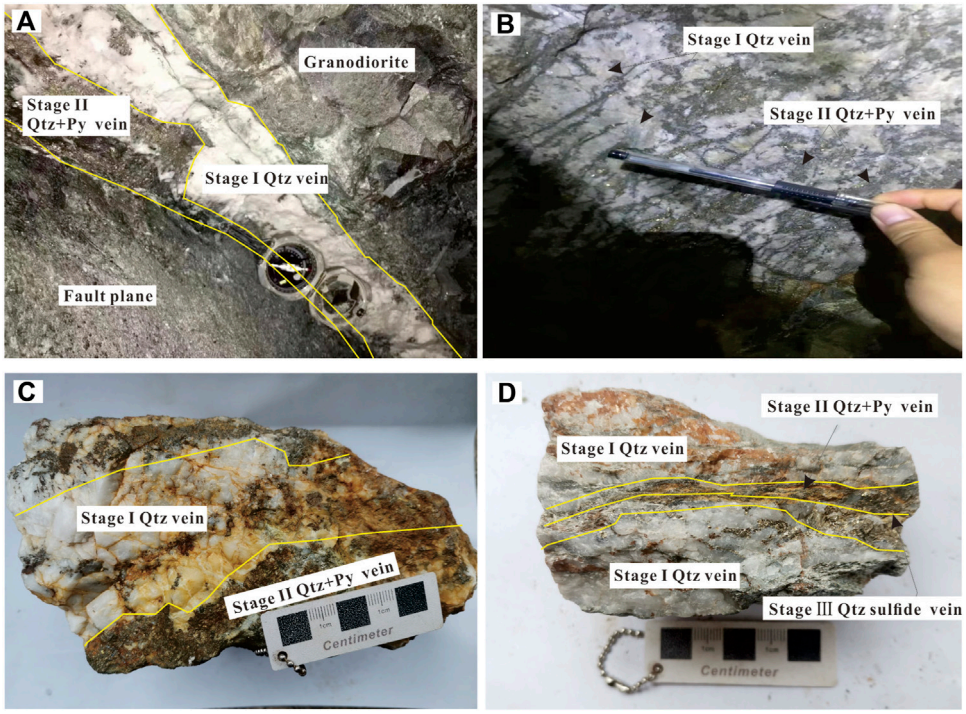

FIGURE 3
Photographs of various mineral assemblages and mineralization stages in the Houge'zhuang gold deposit.

polished to produce thin sections for microscopic observation, back-scattered electron (BSE) scanning microscopy, and *in situ* trace element and sulfur isotope analyses. The pyrite from stage IV was not analyzed in detail.

Fluid inclusion analysis

The fluid inclusion microthermometric experiments were conducted on a Linkam THMS600 heating/cooling stage mounted on a microscope at the Shandong Institute of Geological Sciences (SIGS), Jinan. Liquid nitrogen was used as a coolant and the stage was routinely calibrated at 0 and 374.1°C based on the ice-melting and homogenization temperatures of a pure water synthetic fluid inclusion with the critical density, and at −56.6°C based on the CO_2 melting temperature of a pure CO_2 fluid inclusion, respectively. The estimated uncertainties were ±0.2°C below room temperature and 5°C in the temperature range higher than 200°C, respectively (Bodnar, 1994; Shen et al., 2018; Shu et al., 2020).

The Raman spectroscopic analyses were conducted using a Renishaw inVia Raman microspectrometer at SIGS, with wavelengths of 532 nm and 785 nm. The spectra were recorded at a counting time of ~1 ectrum, with spectra ranging from 0 to 4500cm^{-1} for one accumulation. The salinity and compositions of the fluid inclusions were calculated using the HokieKlincs spreadsheet and algorithms described by Steele MacInnis et al. (2011 and 2016) for H_2O-NaCl and H_2O-CO_2-NaCl systems, respectively.

Electron microprobe analysis

Electron microprobe and element mapping analysis of gold-bearing pyrite was performed at the Jinan Mineral Resources Supervision and Inspection Center at the Ministry of Natural Resources, using a JEOL JXA8230 instrument. The instrument parameters were set with a quantitative acceleration voltage of 15 kV, a beam spot current of 2×10^{-8}A, a beam spot diameter of 0.5 μm, and a data collection time of 20~60s. The ZAF method was used to revise the data and ensure an analysis accuracy of better than 1%. The detection limits were 200 ppm (Fe), 175 ppm (Co), 196 ppm (Ni), 248 ppm (Cu), 281 ppm (Zn), 92 ppm (S), 478 ppm (Pb), 127 ppm (Ti), 235 ppm (Au), 114 ppm (Ag), 328 ppm (Bi), 354 ppm (Se), 144 ppm (Te), 140 ppm (Sb), and 233 ppm (As).

In situ trace element analysis

The *in situ* trace element analyses of gold-bearing pyrite in thin sections were conducted by LA-ICP-MS at the testing center of the Shandong Bureau of China Metallurgical geology bureau.

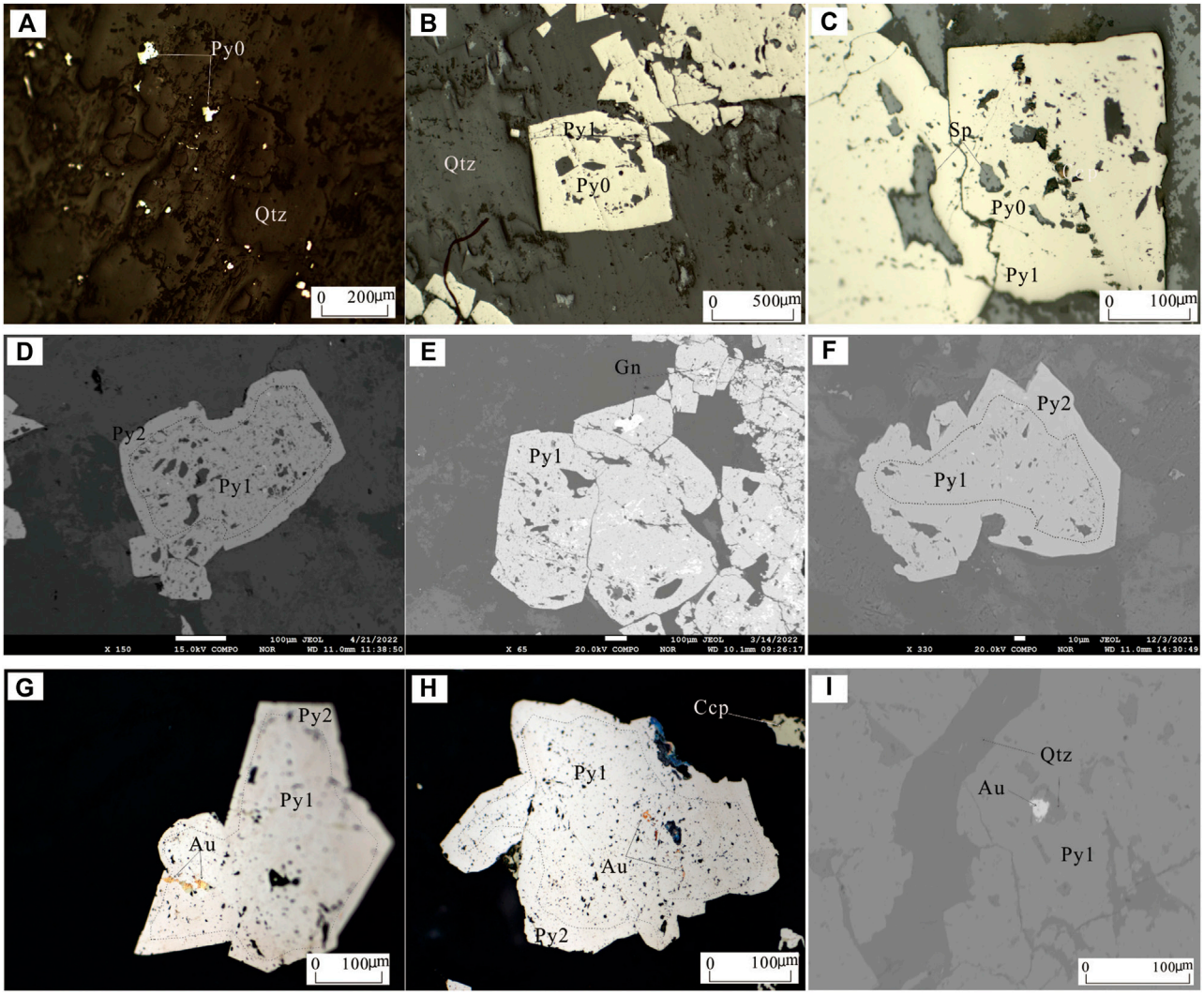

FIGURE 4
Representative reflected-photomicrographs **(A–C)** and backscattered electron (BSE) images. **(D–I)** Occurrences of visible gold and textural features of pyrite.

The GeoLasPro 193 nm ArF excimer system produced by Coherent (USA) was combined with a Thermo Fisher ICAP Q quadrupole ICP-MS for the experiments. The 193-nm ArF excimer laser, homogenized by a set of beam delivery systems, was focused on the mineral surface with a fluence of 10–12 J/cm^2. Each acquisition incorporated a 20 s background (gas blank), followed by a spot diameter of 30 um at a 5 Hz repetition rate for 60 s. Helium (750 ml/min) was applied as a carrier gas to efficiently transport aerosol out of the ablation cell and was mixed with argon *via* T-connector before entering the ICP torch.

The external calibration standards included American National Bureau of Standards and Technology synthetic standard glass, NIST610, and United States Geological Survey basaltic glasses, including GSD-1G and BCR-2G. Raw data were reduced offline by *ICPMSDataCal* software using a normalization strategy without applying an internal standard (Liu et al., 2008). Chinese Geological Standard Glasses MASS-1 were used for quality control.

In situ sulfur isotope analysis

The LA-MC-ICP-MS *in situ* sulfur isotope analysis was performed by the Jinan Mineral Resources Supervision and Inspection Center of the Ministry of Natural Resources on a Neptune Plus multi-receiver plasma mass spectrometer (Thermo Scientific) coupled with a GeoLasPro 193 nm laser ablation

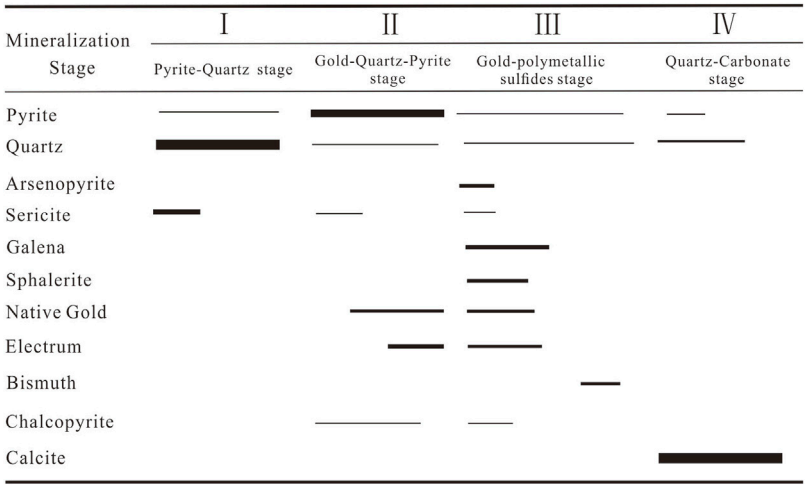

FIGURE 5
Paragenetic sequence of the Houge'zhuang gold deposit. Thick lines: high abundance. Thin lines: low abundance.

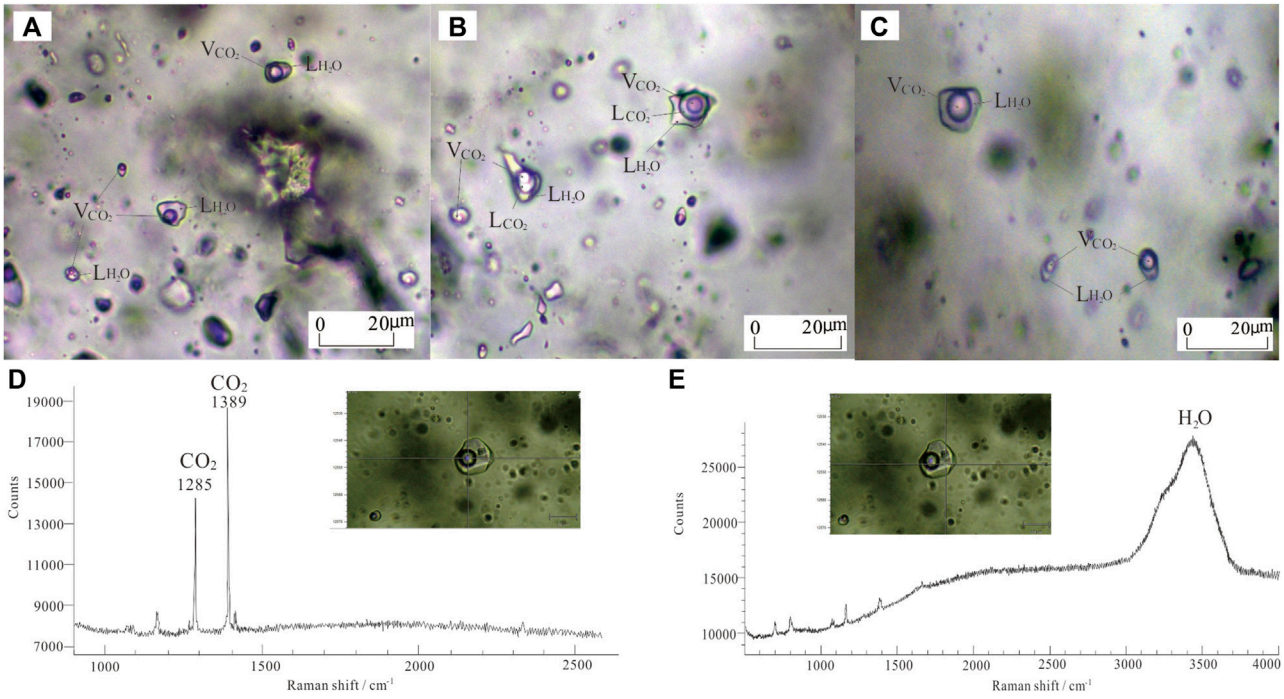

FIGURE 6
Photomicrographs **(A–C)** and laser Raman **(D,E)** spectrogram of fluid inclusions in the Houge'zhuang gold deposit.

system. The appropriate area was selected according to a scanned photo of the sample, and the laser ablation system was used to ablate the sulfide (point ablation). The diameter of the laser beam was 44 μm, with an energy density of 6J/cm^2, a frequency of 6Hz, and high-purity helium as the carrier gas. The sulfide standard samples HN, JX, and ZX were used to debug the instrument parameters. In the analytical process, sulfide similar to the sample matrix was used to replace the standard sample, and the standard-sample-standard crossover method was used for quality discrimination correction.

TABLE 1 Microthermometric measurements of fluid inclusions of different mineralization stages in the Houge'zhuang gold deposit.

Stage of mineralization	Rock type	Fl type	$TmCO_2$/°C	Ti/°C	TCl/°C	Tht/°C	Salinity (wt.%NaCl eq0	Data source
Stage I	Pyrite quartz vein	I	−56.2~−56.3	—	5.3~7.2	309.2~319.8	5.33~8.51	This article
		II	-	−1.6~−4.9	-	146.9~304.6	2.74~7.73	
		III	-	−1.4~−2.1	-	251.7~342.6	2.41~3.55	
Stage II	Gold pyrite vein	I	-	-	7.2~8.1	141.1~227.4	5.33~3.71	
		II	-	−5.7~−2.8		172.7~273.2	4.65~8.81	
		III	−56.1~−56.3	-	7.2~8.3	285.4~332.1	5.33~3.33	
Stage III	Gold-sulfide vein	I, II	-	-	-	211~252	3.58~4.51	Wang et al. (2018)

Tht/°C, homogenization temperature; Ti/°C, last melting temperature of ice; TCl/°C, last melting temperature of hydrohalite; TmCO2/°C, last melting temperature of CO_2.

Results

Fluid inclusion analysis

The fluid inclusions in the Houge'zhuang gold deposit are relatively developed and mainly distributed in transparent quartz grains with growth zoning. The present study primarily selected quartz inclusions from stages I and II of mineralization for testing. Based on the observed phases at room temperature, three types of fluid inclusions were observed from the ores: single-phase (type I), two-phase aqueous (type II) (Figures 6A,C), and CO_2-rich three-phase (type III) (Figure 6B) inclusions. Type I is the predominant type in the Houge'zhuang gold deposit, contributing approximately 40–50% of the total fluid inclusions, which is composed of the pure CO_2 (liquid or vapor) and pure H_2O (liquid or vapor) phases. Most of the type II inclusions are ellipse in shape, with those measuring <6 μm on the long axis accounting for ~20–30% of the total fluid inclusions, with vapor/liquid ratios <30–40%, predominant round and ellipse shapes, and measuring approximately 5–10 μm. The main components of the vapor and liquid in type I are CO_2 and H_2O, respectively. Type III is composed of CO_2 vapor and liquid phases and H_2O liquid phases, with round, ellipse, and irregular shapes ranging in size from 4 to 7 μm. All three types of fluid inclusions were found in stages I, II, and III of mineralization.

The microthermometric results showed that the homogenization temperatures of the fluid inclusions in stage I ranged between 146.9°C and 342.6°C, whereas those for stages II and III were 141.1–332.1°C and ~211 and 252°C, respectively (Table 1). As the CO_2–H_2O inclusions with variable phase ratios were trapped from the immiscible CO_2–H_2O fluids, the lower temperature (~ 141–211°C) was their formation temperature. The salinities in stages I, II, and III were similar, with NaCleq of ~2.74–8.51%, ~ 3.71–8.81%, and ~3.58–4.51%, respectively. These findings suggest that the ore-forming fluids were of medium-low salinity and temperatures.

Furthermore, the results of laser Raman spectroscopy showed that the fluid inclusions were mainly composed of H_2O and CO_2 (Figure 6), while the vapor phases were mainly CO_2, with less CH_4, N_2, H_2S, organic matter, etc.

Pyrite texture and chemical composition

Micro-texture and type of pyrite

The microstructure of pyrite is controlled by multiple factors including the distribution of elements and crystallization conditions (Reich et al., 2005; Large et al., 2009; Cook et al., 2009; Deditius et al., 2014; Peterson and Mavrogenes, 2014; Román et al., 2019; Hu et al., 2020). Increasing contents of trace elements such as As, Co, Ni, and Cu in pyrite can result in different bands in BSE images. Different crystallization conditions can also result in varied microstructures.

Based on microscope observation, BSE images, and element mapping, the pyrites in the Houge'zhuang gold deposit can be divided into three types, Py0, Py1, and Py2, which showed good correspondence with the mineralization stages Figures 7A–C.

Py0: This type is mainly present in pyrite-quartz veins (stage I), and is medium-fine-grained (~10–50 μm) with euhedral to subhedral shapes (Figure 4A). The symbiotic minerals are mainly quartz, with small amounts of sericite. Py0 mainly has two output forms in the gold ore, one of which occurs as single-grain disseminated in quartz veins (Figure 4A); the other form occurs as a core to form new pyrites with later-formed pyrites (Figures 7E,F). Py0 accounted for 10–20% of all pyrites in the gold ore.

Py1: This type occurs in gold-quartz-pyrite veins (stage II), and is coarse-medium-grained (~100–2000 μm) with euhedral to subhedral shapes. Py1 always occurs as aggregates or veins and is spatially associated with visible gold. This type is mainly porous

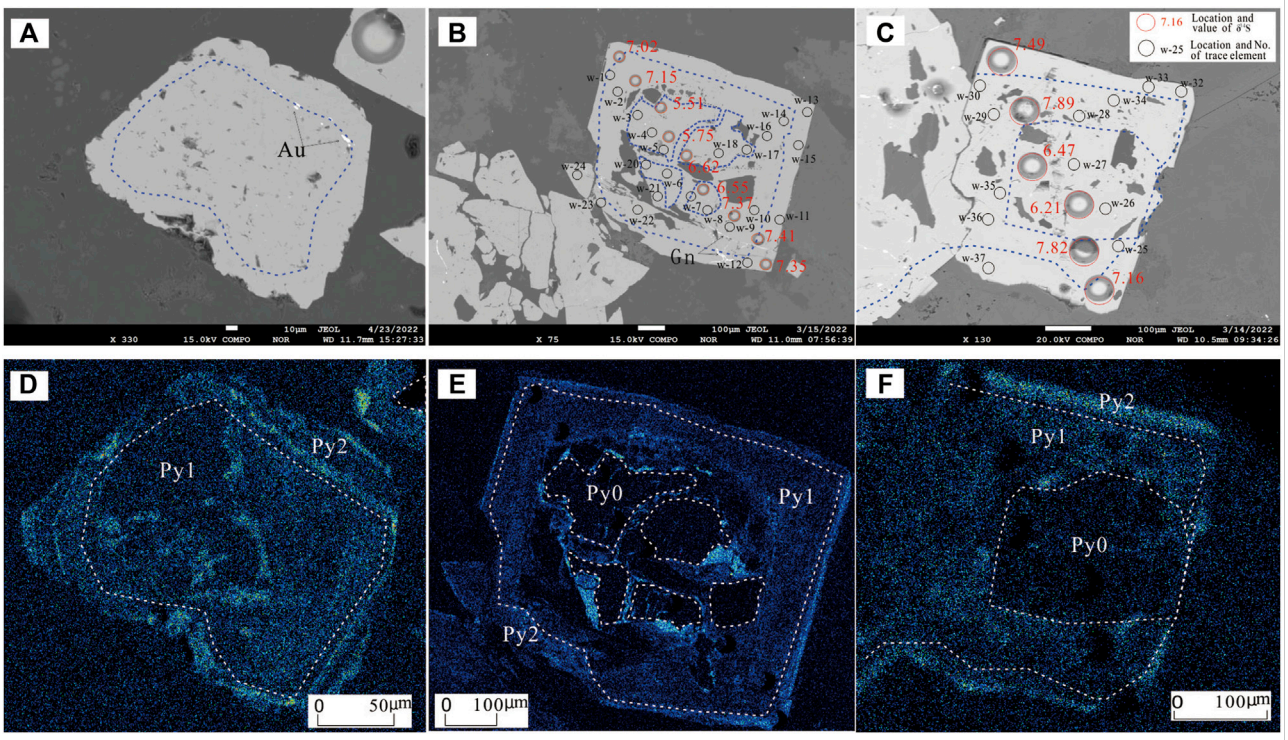

FIGURE 7
Backscattered electron (BSE) images **(A–C)** and element mapping images **(D–F)** of pyrites in the Houge'zhuang gold deposit.

and has a honeycomb structure and metasomatic-relict texture, and displays cataclastic textures due to later stress (Figures 4C–F), with micro-fractures locally filled with visible gold grains (Figures 4G–I). The symbiotic minerals are mainly quartz, chalcopyrite, and visible gold. The element mapping images showed a higher As content in Py1 than that in Py0, but less than that in arsenic-bearing pyrite (Py2) (Figures 7D–F). Py1 accounted for 70–80% of pyrites in the gold ore.

Py2: This type is arsenic-bearing and occurs in quartz-polymetallic sulfide veins (stage III) (Figures 7D,F). Py2 is produced in two forms. The first is characterized by distinctive core-rim textures, showing oscillatory or patchy zoning of arsenic. The core components of Py2 are mainly Py0 or Py1, which were formed early. The other form is independent arsenic-bearing pyrite, with fine-grained (~10–20 μm) distribution. Py2 is usually inter-grown with coarse-grained chalcopyrite, galena, sphalerite, tellurobismuthite, and magnetite, which occur adjacent to the boundary. Different from the gold in Py0 and Py1, the gold in Py2 is invisible, especially nanogold and lattice gold. Py2 accounted for 5–10% of pyrites in the gold ore.

In situ trace elements

Most of the trace elements in the pyrite crystals were classified as siderophile and sulfophile elements and are found in the periodic table between Fe and S. Some elements can readily enter the pyrite crystal lattice in the form of isomorphic substitution. For example, Co and Ni can replace Fe, while As, Se, Te, etc. can replace S in the pyrite crystal lattice. Another possibility is that trace elements such as Au, Ag, Cu, Pb, Zn, etc. occur in pyrite as mechanical mixtures (Bi et al., 2004; Zhang et al., 2014; Guo et al., 2019; Li J. et al., 2020; Chen et al., 2020c).

The results of the LA-ICP-MS trace element analysis of three different pyrite types from different mineralization stages of the Houge'zhuang gold ores are shown in Table 2. A total of 37 points were analyzed, including eight points for Py0, 19 points for Py1, and 10 points for Py2. All representative trace element contents, such as Co, Ni, Cu, Pb, Zn, As, Ag, Sb, Hg, Bi, and Se, showed regular variation in concentration in Py0, Py1, and Py2. Among them, As was the most abundant, with averages of 498 ppm in Py0, 5419 ppm in Py1, and 8113 ppm in Py2, with a gradual increase in concentration from Py0 to Py2. The change in Au concentration was similar to the change in As concentration, with averages of 1.14 ppm in Py0, 2.82 ppm in Py1, and 4.07 ppm in Py2. The calculated Co/Ni ratios were ~0.11–1.46 (average 0.54) in Py0, ~0.03–46.98 (average 7.16) in Py1, and ~0.28–8.79 (average 2.62) in Py2. In addition, all three pyrite types comprised Cu (~81.44–2414 ppm in Py0, ~0.56–726 ppm in Py1, and ~1.51–173 ppm in Py1), Zn

TABLE 2 Representative trace element concentrations (in ppm) of three pyrite types from the Houge'zhuang gold deposit analyzed by LA-ICP-MS.

Sample No.	Type	Co	Ni	Cu	Zn	As	Ag	Sb	Au	Hg	Bi	Pb	Se	Co/Ni
w-3	Py0	0.96	2.40	81.44	8.31	87.88	5.58	4.06	0.18	0.00	0.00	113.54	0.24	0.40
w-4		13.36	18.79	958.34	83.90	24.57	65.53	9.71	0.14	0.00	1.65	5791.07	0.00	0.71
w-18		3.28	15.11	664.22	21.98	14.93	22.55	1.81	0.09	0.01	0.00	26.33	0.00	0.22
w-19		18.48	29.28	2414.91	37.80	148.86	51.61	9.44	0.43	0.04	0.08	165.96	3.18	0.63
w-20		11.51	21.59	587.31	104.75	1598.79	39.33	11.51	5.66	0.26	0.22	1533.98	0.53	0.53
w-26		65.39	44.87	0.00	24.70	586.91	57.73	23.37	0.62	0.00	3.92	3914.61	3.07	1.46
w-27		95.38	351.18	2599.15	87.79	1466.84	70.31	59.08	1.78	0.05	1.11	2437.10	0.24	0.27
w-28		36.00	319.36	1730.80	36.44	36.88	64.15	9.08	0.26	0.00	0.01	192.29	0.00	0.11
w-1	Py1	465.44	200.01	1.03	0.06	5867.05	0.19	1.18	0.97	0.05	0.04	15.52	3.17	2.33
w-2		287.48	6.12	0.56	0.52	9290.97	0.08	0.21	0.18	0.06	0.02	2.49	0.00	46.98
w-5		5.47	8.73	227.26	17.70	4656.00	12.96	41.46	7.21	0.00	0.22	592.42	1.08	0.63
w-6		27.60	49.95	691.26	59.01	8066.78	30.43	34.45	8.34	0.01	0.07	2572.65	0.38	0.55
w-7		375.95	209.71	726.38	44.48	8370.30	30.96	14.62	9.09	0.01	0.28	532.86	0.00	1.79
w-8		171.75	150.78	190.21	8.03	5586.06	86.35	24.05	3.95	0.00	2.10	2938.74	0.00	1.14
w-9		1378.88	86.63	69.46	22.73	5847.85	20.19	5.25	1.98	0.00	0.82	1111.68	0.00	15.92
w-10		1524.58	164.84	2.23	12.24	7690.34	0.31	0.40	0.58	0.14	0.00	4.17	1.30	9.25
w-14		4.77	157.42	1.13	11.94	4387.27	0.57	3.21	0.30	0.16	0.05	17.66	3.42	0.03
w-16		1044.19	37.21	3.77	2.63	8674.15	1.64	6.14	3.25	0.08	0.03	42.60	2.58	28.06
w-17		52.68	55.63	16.16	2.61	5609.36	4.07	6.76	0.94	0.29	0.13	55.51	2.28	0.95
w-22		27.77	32.72	1.43	0.41	4248.24	1.14	2.10	0.56	0.24	0.05	13.56	0.00	0.85
w-24		0.00	408.17	5.48	9.63	1640.20	9.28	2.80	0.43	0.00	0.11	150.75	1.28	0.00
w-25		643.82	244.53	177.23	1.07	5847.32	2.67	6.99	3.22	0.09	0.60	311.31	0.00	2.63
w-29		193.66	176.89	731.99	83.48	2430.24	79.07	20.07	3.53	0.00	6.77	10639.46	0.00	1.09
w-30		427.09	41.94	0.54	0.76	3320.79	0.30	0.61	0.05	0.17	0.00	11.22	1.17	10.18
w-34		25.89	123.75	576.25	30.61	313.04	26.51	13.18	0.66	0.18	0.19	301.99	0.00	0.21
w-35		81.97	6.34	0.00	0.63	6499.52	3.52	8.03	8.01	0.00	0.13	181.75	0.00	12.93
w-36		12.03	27.18	2.99	5.48	4618.93	0.60	0.96	0.29	0.00	0.05	16.31	0.00	0.44
w-11	Py2	81.60	35.74	10.01	14.10	18199.02	1.09	9.09	10.82	0.23	0.12	30.25	0.00	2.28
w-12		391.23	181.09	3.41	8.96	13545.67	0.24	0.43	4.82	0.06	0.00	1.92	1.31	2.16
w-13		364.40	536.98	21.36	13.00	6688.88	0.09	0.22	5.08	0.04	0.04	1.69	0.00	0.68
w-15		491.76	370.84	0.00	10.39	3818.49	0.92	1.81	3.58	0.01	0.06	9.40	1.24	1.33
w-21		24.71	12.61	34.34	462.39	6994.45	9.17	6.03	5.25	0.00	0.18	802.69	0.00	1.96
w-23		91.93	15.10	1.51	1.45	4821.76	0.94	1.26	0.30	0.11	0.02	27.39	1.07	6.09
w-31		652.19	725.78	3.14	1.88	8823.44	0.00	0.09	5.08	0.00	0.00	3.06	0.00	0.90
w-32		315.98	1112.36	11.94	1.92	8396.25	6.41	3.42	1.97	0.14	0.28	565.26	1.51	0.28
w-33		1498.45	170.50	173.09	10.22	7473.56	11.16	11.93	3.45	0.00	0.15	311.02	0.00	8.79
w-37		173.95	98.52	21.92	4.90	2374.04	0.35	0.73	0.37	0.09	0.02	5.72	0.00	1.77

(~8.31–104.75 ppm in Py0, ~0.06–83.5 ppm in Py1, and ~1.45–462.4 ppm in Py1), Ag (~5.58–70.3 ppm in Py0, 0.08–86.4 ppm in Py1, and ~0.09–11.1 ppm in Py2), and Pb (~26.3–5791 ppm in Py0, 2.49–10639 ppm in Py1, and ~1.69–802.69 ppm in Py2).

The comparative trace element concentrations of the three pyrite types are illustrated in boxplots (Figure 8), showing the relative variations in trace elements in different types of pyrite grains. Co, Ni, and As were enriched in Py2, with an increasing trend from Py0 to Py2, similar to Au, indicating their close relationship to gold mineralization. The ore elements, such as Zn, Pb, Cu, Ag, Sb, and Bi, were enriched in Py0 and depleted in Py2 relative to Py1, with a downward concentration trend contrary to that in Au.

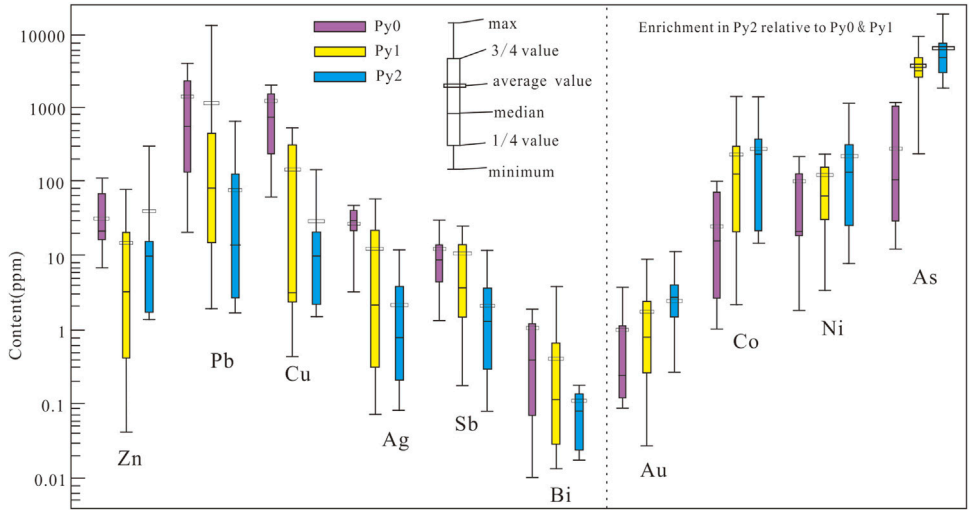

FIGURE 8
Comparative box plot of trace element concentrations in the three pyrite types.

Elemental mapping of pyrite

Electron microprobe mapping plays an important role in the study of element distributions. Element microprobe mapping analysis can intuitively reveal the combinations and spatial distributions of major, minor, and trace elements in pyrites at different stages. Thus, pyrites formed at different stages can be identified and used to study the evolution of ore-forming fluids (Chi et al., 2020).

The pyrite of stage III was selected for EMPA element mapping to reveal the distribution and correlation of the major and trace elements (Figures 7D–F). The As content in the core of the pyrite crystals was relatively low, with clear boundaries (Figures 7B,C), and was distributed irregularly in the intermediate part of the Py0 pyrite. In contrast, the As content at the edge of the pyrite crystal was significantly higher than that at the core of the pyrite and showed irregular oscillatory zoning (Py1). At the extreme edge of the pyrite, the As content increased significantly and was distributed in intermittent bands, forming arsenic-bearing pyrite (Py2). Therefore, according to the As concentration, the pyrite related to gold mineralization in the Houge'zhuang gold deposit can be divided into Py0, Py1, and Py2. Py0 with low As concentration and without obvious zoning occurred mainly in the core of pyrite crystals and was formed in stage I. Py1, with a higher As concentration than that in Py0, showed oscillating zoning and was formed in stage II. In contrast, Py2 occurred mainly at the crystal edge, with the highest As concentration, and was formed in stage III.

Gold distribution

The microscopic observations, BSE images, and EPMA mapping findings showed that the gold in the Houge'zhuang deposit was distributed in the pyrite interstice, fissures, and within pyrite crystals, while the rest was invisible gold (particularly nanogold and lattice gold).

Gold mainly occurred in stages II and III, but in different ways. Stage II showed a high amount of readily visible gold along with pyrite fissures (Figures 4G,H) distributed throughout the interstice and quartz inclusions (Figure 4I). The most common form was native gold, with bright golden yellow color, granular texture, and mainly fine particles (~5–30 μm). The other type was electrum, which had an irregular fine-grained and granular texture and a low amount of natural gold in comparison. In contrast to stage II, the gold in stage III was mainly invisible gold, such as nanogold and lattice gold, and was closely associated with arsenic-bearing pyrite (Py2) and arsenopyrite. Nanogold or fine-grained gold (~1–5 μm) was scattered in Py2. The lattice gold was most likely to be present in the lattice of the arsenic-bearing pyrite.

Sulfur isotopic compositions of pyrite

Sulfur isotopes are sensitive indicators of the source and migration process of ore-forming fluids and the genesis of ore deposits. These isotopes are often used to depict the physical and chemical conditions of petrogenesis and mineralization and the source of sulfur.

TABLE 3 Results of the *in situ* analysis of sulfur isotopes of pyrite in the Houge'zhuang gold deposit.

Sample No.	Type	$\delta^{34}S_{v\text{-}CDT}$	Average value	Sample No.	Type	$\delta^{34}S_{v\text{-}CDT}$	Average value
HGZ-1-04	Py0	6.55	6.28	HGZ-1-02	Py1	7.41	7.44
HGZ-1-05		6.62		HGZ-1-03		7.37	
HGZ-1-06		5.75		HGZ-1-08		7.15	
HGZ-1-07		5.51		HGZ-2-02		7.89	
HGZ-2-03		6.47		HGZ-2-05		7.82	
HGZ-2-04		6.21		HGZ-2-1_02		7.52	
HGZ-2-2_01		6.86		HGZ-2-1_03		7.62	
HGZ-1-01	Py2	7.35	7.45	HGZ-2-1_04		7.46	
HGZ-1-09		7.02		HGZ-2-1_05		7.38	
HGZ-2-01		7.49		HGZ-2-1_06		7.13	
HGZ-2-06		7.16		HGZ-2-1_09		7.30	
HGZ-2-1_01		7.58		HGZ-2-2_03-1		7.30	
HGZ-2-1_07		7.84		HGZ-2-2_03-2		7.33	
HGZ-2-1_08		7.46		HGZ-2-2_04		7.63	
HGZ-2-2_02		7.23		HGZ-2-2_04'		7.26	
HGZ-2-2_03		7.95					

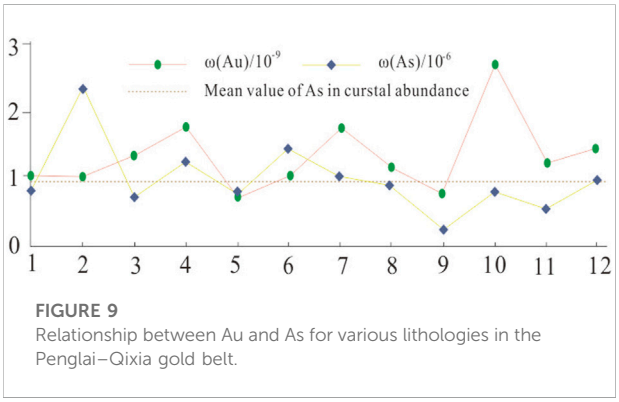

FIGURE 9
Relationship between Au and As for various lithologies in the Penglai–Qixia gold belt.

The results of *in situ* sulfur isotope analysis on the cores and different zones of gold-bearing pyrite crystals in this study are shown in Table 3. *In situ* analyses were performed on Py0 (N = 7), Py1(N = 15), and As-rich rim in Py2 (N = 9).

The $\delta^{34}S$ values of Py0 formed in stage I ranged from 5.51 to 6.86‰ (mean 6.28‰), those of Py1 formed in stage II ranged from 7.13 to 7.89‰ (mean 7.44‰), and those of Py2 formed in stage III ranged from 7.02 to 7.95‰ (mean 7.45‰), similar to that of Py1. Grain-scale variations in $\delta^{34}S$ in the pyrite grains were observed (Figures 7B,C). As shown in Figure 7B, the core (Py0) had $\delta^{34}S$ values of ~5.51–6.62‰, which increased to ~7.15–7.49‰ on the rim (Py1 and Py2). The $\delta^{34}S$ values of Py2 were slightly higher than those in Py1. These findings are in good agreement with the results obtained by LA-MC-ICP-MS on another pyrite grain (Figure 7C). The range of $\delta^{34}S$ values at the Houge'zhuang gold deposit was similar to those of other gold deposits in Jiaodong.

The grain-scale variations in sulfur isotopic compositions were small but regular, noticeably in pyrite from stages I and III. A rough, positive correlation was observed between the As content and $\delta^{34}S$ value.

Discussion

Characteristics of the ore-forming fluid

Immiscibility during fluid evolution is an important factor for the mineralization of certain metals. For example, immiscible fluid inclusions are frequently observed in contemporaneous quartz formed during the precipitation stage of large amounts of gold. Furthermore, physical and chemical experimental studies have confirmed that fluid immiscibility is beneficial for gold precipitation. The fluid inclusion types, quantities, homogenization temperature, and densities have similarities and differences, reflecting the evolution of ore-forming fluids (Ramboz et al., 1982; Roedder, 1984; Shepherd and Chenery, 1995; Lu et al., 2004).

The results of fluid inclusion studies and laser Raman spectroscopy suggest that the ore-forming fluid in different stages of the Houge'zhuang gold deposit exhibited chemical and physical properties similar to those in the other Jiaodong gold deposits (Hou et al., 2007b; Ma et al., 2015). The homogenization temperatures of the fluid inclusions gradually

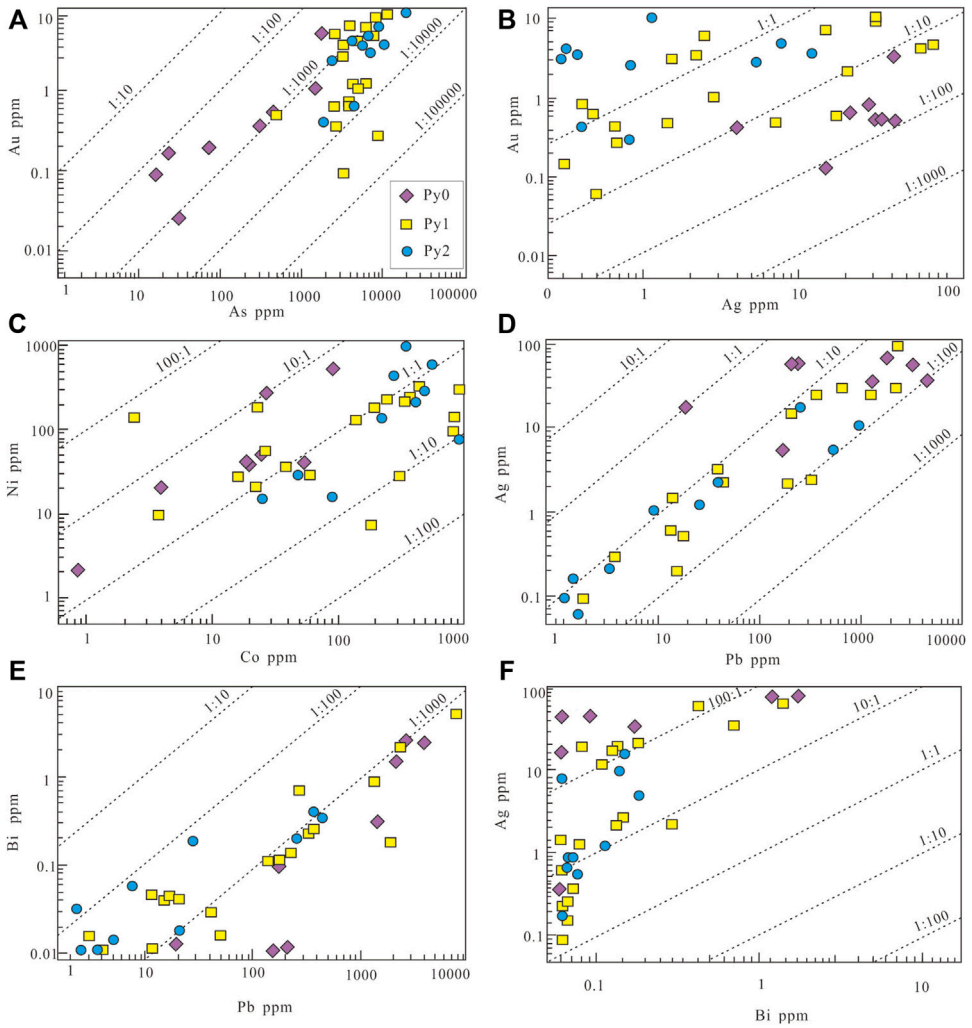

FIGURE 10
Binary plots of **(A)** Au *vs.* As, **(B)** Au *vs.* Ag, **(C)** Bi *vs.* Co, **(D)** Ag *vs.* Pb, **(E)** Bi *vs.* Pb, and **(F)** Ag *vs.* Bi in Py0, Py1, and Py2 from the Houge'zhuang gold deposit.

decreased from stages I to III and the type combinations of the fluid inclusions also changed. Combined with the results of the salinity analysis, the fluid inclusions in stage I were the fluid from the later stage of magmatic evolution, with high temperature—especially Type III fluid inclusions. In stages II and III, type III fluid inclusions decreased—especially type II fluid inclusions. The homogenization temperature was lower than that in stage I, indicating the evolution of the fluid post-phase separation and immiscibility. The evolution process plays an important role in gold precipitation.

The ore-forming fluids of the Houge'zhuang gold deposit were of medium-low salinity and temperatures, with H_2O and CO_2 being the predominant fluid inclusion components, and CO_2 being the predominant vapor phase component.

As enrichment mechanism

Sources of As fluid

The *in situ* trace element analysis revealed that the content of As, the most abundant trace element, gradually increased from Py0 to Py2 (498 ppm, 5419 ppm, and 8113 ppm, respectively) (Table 2). A clear paragenetic succession for various types of pyrite was observed in the elemental mapping (Figures 7D–F).

Py0 was characterized by low concentrations of As and Au, indicating that the initial hydrothermal fluids may not contain high concentrations of As and Au, which are not the main ore-forming fluids. In Py1, the concentration of As increased significantly, with a relatively uniform distribution and no obvious zonal growth, but notably more fine gold and chalcopyrite inclusions, indicating that fluids with high As and Au were the main ore-forming fluids.

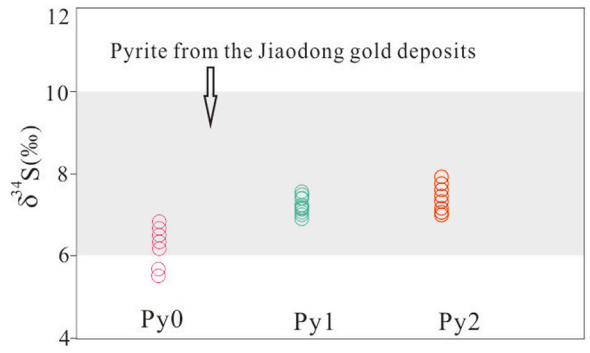

FIGURE 11
Variations in sulfur isotope compositions of various generations of pyrite in the Houge'zhuang gold deposit.

Relative to Py1, Py2 exhibited distinct As enrichment, with As-rich rims of pyrite and growth zoning but a smaller proportion of Py2. This phenomenon implied a lower content of the ore-forming fluid and is indicative of the direct precipitation of Py2 from As-Au-rich solutions.

Regarding the mechanism and source of As enrichment, two main theories have been proposed. First, they could directly precipitate from extremely As-rich auriferous fluids (Barker et al., 2009; Muntean et al., 2011; Peterson and Mavrogenes, 2014). Second, during the fluid migration process, the ore-forming fluid may react with As-rich sedimentary or metamorphic rocks to extract As, becoming more enriched, especially in Carlin-type gold deposits (Ilchik and Barton et al., 1997; Feng et al., 2018; Feng et al., 2020; Large et al., 2014).

The ore-forming fluids of the gold deposits in Jiaodong are mainly As-poor fluids, which are rare. Compared to the other gold belts in Jiaodong, the Penglai–Qixia gold belt developed many Proterozoic Jingshan, Fenzishan, and Penglai groups. Our analysis of the As content in the formation revealed As concentrations in the Fenzishan and Jingshan groups of 11.72 ppm and 2.27 ppm, respectively (Tian et al., 2022), both of which were higher than the average value (0.97 ppm) of the Jiaodong crust (Figure 9). Further considering the discovery of As-rich (~0.4–2.5%) pyrite in the surrounding Heilan'gou and Daliu'hang gold deposits, the primary ore-forming fluids may pass through some As-rich sedimentary rocks such as the Jingshan, Fenzishan, and Penglai groups, resulting in stable water-rock interaction, extraction, and enrichment of As.

Implications for gold mineralization

In hydrothermal gold deposits, pyrite is the main gold-bearing mineral, as the coupling relationship between Au and As has been widely recognized. Most scholars believe that this is the result of As controlling Au enrichment and that the same relationship exists in the Jiaodong gold deposits. The binary plots

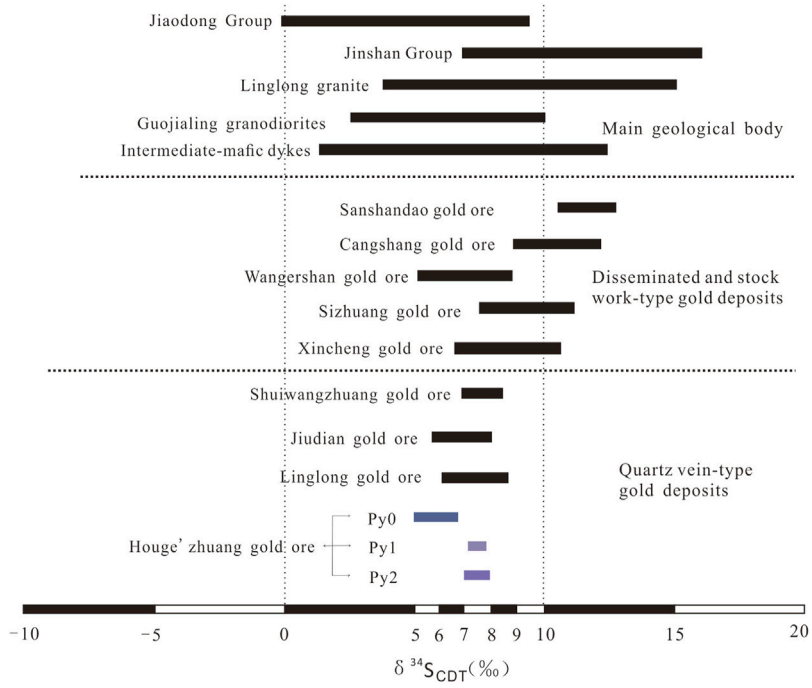

FIGURE 12
Sulfur isotope composition of Jiaodong group metamorphic rocks, granites, dykes, and ores of gold deposits in the northwestern Jiaodong area.

TABLE 4 Sulfur isotopes of typical gold deposits in North Jiaodong.

Area	Deposit name	Deposit type	Object	δ34S Value ‰)	δ34S average value (‰)	Number	Source
Jiao Xibei	Sanshandao	Disseminated-style	Py	11.0~12.6	12.2	7	Wang et al. (2002)
	Cangshang		Py	9.6~12.0	10.8	4	Huang (1994)
	Wangershan		Py	4.8~8.9	6.3	30	Guo et al. (2019)
	Sizhuang		Py	7.1-11.5	9.5	16	Yang et al. (2014)
	Xincheng		Py	7.9~10.7	9.8	18	Li et al. (2020b)
				6.63~9.65	7.61	12	Songet al., 2015
	Jiaojia		Py	7.5~11.46	9.61	15	Songet al., 2015
				7.71~12.58	10.32	12	Jiang (2020)
	Shuiwangzhuang	Quartz vein-style	Py	7.0~8.5	7.7	7	Zhang et al. (2018a)
	Linglong		Py	6.4~8.6	7.6	16	Hou et al. (2006)
	Jiudian		Py	5.7~8.1	7.4	14	Wang et al. (2002)
Penglai–Qixia	Heilan'gou	Quartz vein-style	Py	6.6~8.8	7.2	68	Feng et al. (2018)
				5.5~7.8	6.7		Yan et al. (2014)
				6.3~9.5	7.5	8	Hou et al. (2007a)
	Daliuhang		Py	3.7~8.3	7.1	62	Feng et al. (2020)
	Majiayao		Py	5.5~8.6	6.37		Tian et al. (2020)
	Hexi		Py	5.4~8.8	6.95	17	Hou et al. (2004)

of Au *vs.* As showed a good linear relationship (Figure 10A) and good correlations in different lithologies in Jiaodong (Figure 9).

The ore-forming fluids of the Houge'zhuang gold deposit showed medium-low salinity and temperatures, suggesting that Au may migrate mainly as $Au(HS)^{-2}$ complex (Benningand Seward, 1996; Stefánsson and Seward, 2004; Williams-Jones et al., 2009; Yang et al., 2016b; Chai et al., 2017).

The porous and honeycomb structures and the metasomatic relict texture of the Py1 indicated that fluid boiling occurred due to pressure/temperature changes and a continuous water-rock interaction, consistent with an altered rock-type mineralization mechanism. The water-rock interaction changes the physicochemical conditions, causing the $Au(HS)^{-2}$ complex to destabilize and precipitate Au. The visible gold is the paragenesis gold in Py1.

The difference between Py2 (arsenic-bearing pyrite) and Py1 suggests two distinct ore-forming fluids Figures 10B–F. The gold in Py2 was invisible gold, especially nanogold and lattice gold. Au atoms sit at the Fe atom sites in the As-bearing pyrite structure; moreover, Au and As in As-bearing pyrite are the most abundant chemically bound Au^{+} and As^{-}, respectively. Au^{+} and $As^{-}$are both structurally bound and sit at the Fe and S atom sites of pyrite, respectively; wherein As^{1-} changes the crystal structure of pyrite, rendering it easy for Au^{1+} to replace Fe^{2+}(Palenik et al., 2004; Kusebauch et al., 2019; Xing et al., 2019; Meng et al., 2022), resulting in the formation of lattice gold. The enrichment of As in pyrite may lead to high partition coefficients for Au between fluid and pyrite, which can effectively adsorb Au-HS complexes from the fluid onto the As-bearing pyrite growth interface through chemical adsorption, resulting in nanogold formation.

The analysis revealed that Au was closely associated with As. Fine and coarse visible gold grains tended to occur in association with the Py1 of stage II, while invisible gold was related to the Au-As-rich Py2 of stage III. These As-bearing pyrites showed a close spatiotemporal relationship to gold, thus playing an important role in the formation and exploration of high-grade gold deposits.

Sources of sulfur and ore metals

The sulfur isotope ratios of the sulfides that co-precipitated with gold have been used as a reliable measure to determine the source of gold, as gold commonly complexes with sulfide as $Au(HS)^{2-}$ in hydrothermal fluids (Hayashi and Ohmoto 1991; Benning and Seward, 1996; Stefansson and Seward, 2004; Williams-Jones et al., 2009).

The *in situ* sulfur isotope values of pyrite measured in the present study were relatively stable, with a narrow variation ($\delta^{34}S_{CDT}$ = ~ 5.51–7.95‰), showing a tower effect and a positive deviation from meteorite sulfur, similar to the other deposits in Jiaodong (Hou et al., 2007a; Yan et al., 2014; Wang et al., 2015; Wen et al., 2016; Feng et al., 2018; Yang et al., 2018; Chai et al., 2020b).

Grain-scale variations were observed in $\delta^{34}S$ in pyrite grains. The core (Py0) had $\delta^{34}S$ values of ~5.51–6.62‰, increasing to

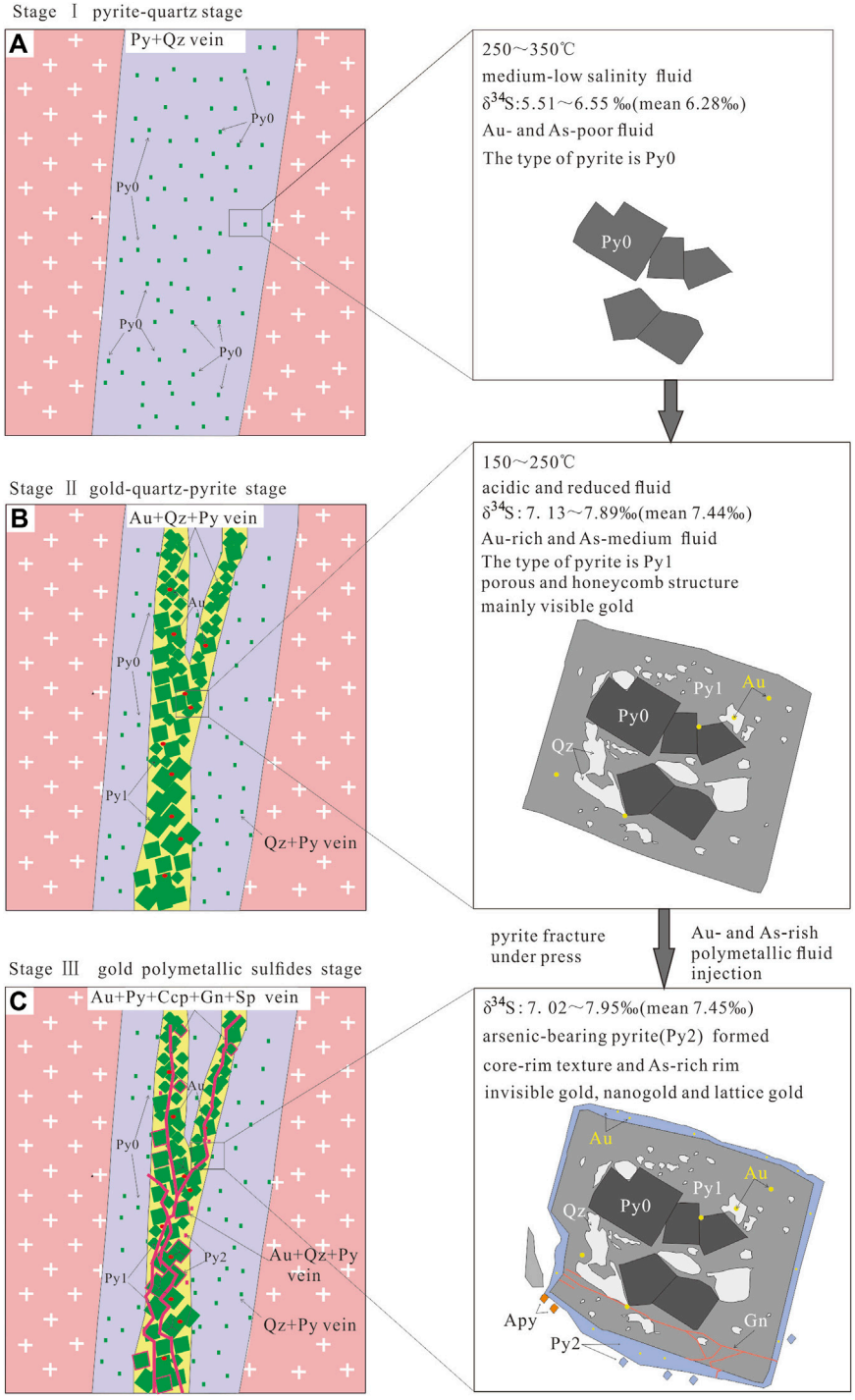

FIGURE 13
Gold metallogenic process of Houge'zhuang gold deposit for different mineralization stages.

~7.15–7.49‰ on the rim (Py1 and Py2). The $\delta^{34}S$ values of Py2 were slightly higher than those in Py1. The results indicated that the sulfur isotopes in Py1 and Py2 were highly homogenized and shared the same sources, while the sources of Py0 differed (Figure 11).

These $\delta^{34}S$ values were comparable to those from the Jiaodong and Jingshan groups, Linglong granite, Guojialing granodiorite, and certain basic dykes (Figure 12; Table 4). However, these $\delta^{34}S$ values were closer to those from the granite country rocks and the Precambrian metamorphites,

indicating that the sulfur in the gold deposits was inherited from these country rocks. Basic dykes showed a close spatiotemporal relationship to the gold deposits; however, due to their small scale, the basic dykes were insufficient to provide such a large amount of sulfur.

The Py0 in stage I had relatively low $\delta^{34}S$ values, ranging from 5.51 to 6.62‰ (mean of 6.28‰), which were like those of pyrite from the potassic zone ($\delta^{34}S$, mean of 7.1‰) and Guojialing granodiorite ($\delta^{34}S$, mean of 6.7‰; Wang et al., 2002). These similar sulfur isotopic compositions may indicate one major source of early fluids.

Compared to Py0, Py1 and Py2 showed higher $\delta^{34}S$ values (mean 7.45‰ and 7.44‰, respectively). Mass fractionation during the precipitation of pyrite cannot account for these elevated $\delta^{34}S$ values; rather, an external ^{34}S-rich fluid injection is likely. The $\delta^{34}S$ values of Py1 and Py2 were similar to those of the Jingshan group (8.2–12.0‰, average 9.7‰; Zhang, 1999), which is located around the Houge'zhuang gold deposit, indicating that some sulfur from the Jingshan group leached into the ore-forming fluid. This conclusion is also supported by elevated As and Au concentrations in ore-related pyrite (Feng et al., 2018; Feng et al., 2020), in which the ore-forming fluids passed through some $\delta^{34}S$-rich sedimentary rocks, leading to $\delta^{34}S$-enriched fluid.

Comprehensive analysis suggested that the sulfur in the Houge'zhuang gold deposit originated from mixed sulfur sources, especially the Jiaodong metamorphic basement and Mesozoic granite wall rocks, with precipitation of magmatic sulfur from the mantle and surface.

Au mineralization process in the Houge'Zhuang gold deposit

Pyrite is the most important ore and gold-bearing mineral in the Jiaodong gold deposits. Its precipitation process extends from the early gold mineralization stage to the late stage; thus, exploring the structural element and isotope changes of pyrite at the microscopic scale aids in understanding its complex growth history, accurately determining the source of ore materials, and providing an in-depth understanding of the mineralization process (Ogryzlo, 1935; Helgeson and Garrels, 1968; Henley, 1973; Renders and Seward, 1989; Wood, 1989; Hayashi and Ohmoto, 1991; Seward, 1991; Gammons and Williams Jones, 1995; Zotov et al., 1996; Archibald et al., 2002; Reich et al., 2005; Large et al., 2009; Wu et al., 2019a; Kusebauch et al., 2019).

The results of previous comprehensive studies on the fluid inclusions, *in situ* S isotope analysis, *in situ* LA-ICP-MS trace element analysis, and electron microprobe mapping analysis of the gold-bearing pyrite have shown that the Houge'zhuang gold deposit was formed during the evolution of multi-stage ore-forming fluids.

In stage I, the fluid was acidic and weakly reducing under medium-high temperature conditions (~250–350°C), while the Au and As content in the fluid was relatively low and only a small amount of gold was precipitated. The Py0 formed at this stage was medium-fine-grained. The $\delta^{34}S$ values of Py0 ranged from 5.51 to 6.86‰ (mean value 6.28‰) (Figure 13A).

In stage II, the main stage of gold mineralization, the ore-forming fluids flowed through some $\delta^{34}S$ and As-rich sedimentary rocks and were supersaturated with high sulfur fugacity at ~150–250°C. Fluid inclusion data showed that Au was dissolved and transported as gold bisulfide [$Au(HS)^0$, $Au(HS)^{2-}$)] (Shu et al., 2020). As the pressure of the ore-forming fluid decreased, it boiled, changing the physicochemical conditions and destabilizing the $Au(HS)^{2-}$ complex, resulting in the precipitation of visible gold and simultaneous Py1 formation (Figure 13B).

During the gold polymetallic sulfide stage (III), new ore-forming fluids formed in the deep, with a lower content than stage II but rich in polymetals. The ore-forming fluids passed through some As-rich sedimentary rock, resulting in fluid enriched with As. During this stage, with the precipitation of As-rich fluid and deep-circulating meteoric water, the physicochemical property of the ore-fluid changed from weakly acidic oxidation to weakly acidic reduction. During fluid migration, with changes in temperature and pressure, As^{1-} sat at the atom sites of S^{2+}, which changed the crystal structure of pyrite, rendering it easy for Au^{1+} to replace Fe^{2+}. Moreover, As enrichment in pyrite can lead to high partition coefficients for Au between fluid and pyrite, which can effectively adsorb Au-HS complexes from the fluid into the As-bearing pyrite growth interface through a chemical adsorption mechanism, resulting in the formation of nanogold and lattice gold. Meanwhile, H_2S and metal ions such as Fe^{2+}, Zn^{2+}, Pb^{2+}, and Cu^{2+} in the ore-forming hydrothermal fluid are consumed, forming metal sulfides such as sphalerite, galena, chalcopyrite, and arsenopyrite. Py2 (arsenic-bearing pyrite) is also formed during this period (Figure 13C).

In stage IV, the temperature of the injected fluid and oxygen and sulfur fugacity were low, while the gold content in the fluid was insufficient for mineralization.

Conclusion

1) Three types of fluid inclusions were identified from the ores: single-phase inclusions (type I), two-phase aqueous inclusions (type II), and CO_2-rich three-phase inclusions (type III). The ore-forming fluids of the Houge'zhuang gold deposit exhibited medium-low salinity and temperatures. The fluid inclusions were composed mainly of H_2O and CO_2, while the vapor phases were mainly CO_2.
2) The pyrite in the Houge'zhuang gold deposit can be divided into three types: Py0, Py1, and Py2, which showed good correlations with the mineralization stages. Py0 was

characterized by low concentrations of As and Au and low $\delta^{34}S$ values (5.51–6.86‰). Py1, hosted in the gold-quartz-pyrite veins, was chemically homogeneous with no obvious zonal growth but with significantly more gold and chalcopyrite inclusions. Py1 contained medium and uniform concentrations of As and Au and had $\delta^{34}S$ values ranging from 7.13 to 7.89‰ (mean 7.44‰). Py2, the arsenic-bearing pyrite, was hosted in quartz-polymetallic sulfide veins and showed distinct As enrichment with As-rich rims of pyrite and growth zoning.

3) The primary ore-forming fluids may pass through some As-rich sedimentary rocks, extracting and enriching As. Au was closely associated with As. Fine and coarse visible gold grains tended to occur in association with the Py1 of stage II, while invisible gold was related to the Au-As-rich Py2 of stage III.
4) The results of comprehensive analyses suggest that the sulfur in the Houge'zhuang gold deposit originated from mixed sulfur sources, especially from the Jiaodong metamorphic basement and Mesozoic granite wall rocks, with the participation of magmatic sulfur from the mantle and surface.
5) The gold metallogenic process of the Houge'zhuang gold deposit indicates that the deposit was formed during the evolution of multi-stage ore-forming fluids.

Data availability statement

The original contributions presented in the study are included in the article/Supplementary material. Further inquiries can be directed to the corresponding author.

Author contributions

NC, ZH, and CL wrote the manuscript. WZ, WS, YZ, and ZL revised the manuscript, conceived the experiments, and contributed to the data interpretation. The fieldwork and preliminary study of samples were carried out by ML and XW. YS conducted the geochemical analyses and reviewed both the science and English language. All authors have read and agreed to the published version of the manuscript.

Funding

The study was supported by the Natural Science Foundation Project of Shandong Province (grant numbers ZR2019PD019, ZR2020QD029, and ZR2020MD039).

Acknowledgments

The authors thank Shen Kun, who is 83 years old this year and still working in geology. His ideas and insights were very helpful. They acknowledge the efforts of the reviewers, which significantly improved the manuscript. They also thank the Natural Science Foundation of China for supporting our research (grant numbers 42172094, 42203034, and 42272122).

Conflict of interest

The authors declare that the research was conducted in the absence of any commercial or financial relationships that could be construed as a potential conflict of interest.

Publisher's note

All claims expressed in this article are solely those of the authors and do not necessarily represent those of their affiliated organizations, or those of the publisher, the editors, and the reviewers. Any product that may be evaluated in this article, or claim that may be made by its manufacturer, is not guaranteed or endorsed by the publisher.

References

ArchibaldMigdisov, S. A. A., and Williams-Jones, A. E. (2002). An experimental study of the stability of copper chloride complexes in water vapor at elevated temperatures and pressures. *Geochimica Cosmochimica Acta* 66 (9), 1611–1619. doi:10.1016/s0016-7037(01)00867-5

Arehart, G. B., Chryssoulis, S. L., and Kesler, S. E. (1993). Gold and arsenic in iron sulfides from sediment-hosted disseminated gold deposits-implications for depositional processes. *Econ. Geol.* 88, 171–185. doi:10.2113/gsecongeo.88.1.171

Barker, S. L., Hickey, K. A., Cline, J. S., Dipple, G. M., Kilburn, M. R., Vaughan, J. R., et al. (2009). Uncloaking invisible gold: Use of nanoSIMS to evaluate gold, trace elements, and sulfur isotopes in pyrite from carlin-type gold deposits. *Econ. Geol.* 104, 897–904. doi:10.2113/gsecongeo.104.7.897

Benning, L. G., and Seward, T. M. (1996). Hydrosulphide complexing of Au (I) in hydrothermal solutions from 150–400 °C and 500–1500 bar. *Geochim. Cosmochim. Acta* 60, 1849–1871. doi:10.1016/0016-7037(96)00061-0

Bi, X. W., Hu, R. Z., and Peng, J. T. (2004). REE and HFSE geochemical characteristics of pyrites in yao'an gold deposit: Tracing ore forming fluid signatures. *Bull. Mineralogy' Petrology Geochem.* 23 (1), 1–4.

Bodnar, R. J. (1994). Synthetic fluid inclusions: XII. The system H_2O-NaCl. Experimental determination of the halite liquidus and isochores for a 40 wt.% NaCl solution. *Geochimica Cosmochimica Acta* 58 (3), 1053–1063. doi:10.1016/0016-7037(94)90571-1

Chai, P., Hou, Z. Q., Zhang, H. R., and Dong, L. L. (2019b). Geology, fluid inclusion, and H–O–S–Pb isotope constraints on the mineralization of the xiejiagou gold deposit in the jiaodong peninsula. *Geofluids* 2019, 3726465. doi:10.1155/2019/3726465

Chai, P., Hou, Z. Q., and Zhang, Z. Y. (2017). Geology, fluid inclusion and stable isotope constraints on the fluid evolution and resource potential of the xiadian gold deposit, jiaodong peninsula. *Resour. Geol.* 67, 341–359. doi:10.1111/rge.12134

Chai, P., Zhang, H. R., Dong, L. L., and Zhang, Z. Y. (2019c). Geology and ore-forming fluids of the dayingezhuang gold deposit, jiaodong peninsula, eastern China: Implications for mineral exploration. *J. Geochem. Explor.* 204, 224–239. doi:10.1016/j.gexplo.2019.06.001

Chai, P., Zhang, H. R., Hou, Z. Q., and Zhang, Z. Y. (2020a). Geochronological framework of the Damoqujia gold deposit, Jiaodong Peninsula, China: Implications for the timing and geologic setting of gold mineralization. *Geol. J.* 55, 596–613. doi:10.1002/gj.3428

Chai, P., Zhang, H. R., Hou, Z. Q., Zhang, Z. Y., and Dong, L. L. (2020b). Ore geology, fluid inclusion, and stable isotope constraints on the origin of the Damoqujia gold deposit, Jiaodong Peninsula, China. *Can. J. Earth Sci.* 57, 1428–1446. doi:10.1139/cjes-2018-0247

Chai, P., Zhang, Z. Y., and Hou, Z. Q. (2019a). Geological and fluid inclusion constraints on gold deposition processes of the dayingezhuang gold deposit, jiaodong peninsula, China. *Acta Geol. sinica-. Engl. Ed.* 93 (4), 955–971. doi:10.1111/1755-6724.13849

Chen, F. C., Deng, J., Wang, Q. F., Jan, F. C., Deng, J., Wang, Q. F., et al. (2020c). LA-ICP-MS trace element analysis of magnetite and pyrite from the Hetaoping Fe-Zn-Pb skarn deposit in Baoshan block, SW China: Implications for ore-forming processes. *Ore Geol. Rev.* 117, 103309–103317. doi:10.1016/j.oregeorev.2020.103309

Chi, N. J., Han, Z. Z., and Shan, W. (2020). Typomorphic characteristics of gold-bearing pyrite in jiaojia fault deep zone of northwest jiaodong peninsula and its geological significance. *Acta Geosci. Sin.* 41 (6), 949–962. doi:10.3975/cagsb.2020.070101

Chouinard, A., Paquette, J., and Williams-Jones, A. E. (2005). Crystallographic controls on trace-element incorporation in auriferous pyrite from the Pascua epithermal high-sulfidation deposit, Chile-Argentina. *Can. Mineralogist* 43, 951–963. doi:10.2113/gscanmin.43.3.951

Cook, N. J., Ciobanu, C. L., and Mao, J. W. (2009). Textural control on gold distribution in as-free pyrite from the dongping, huangtuliang and hougou gold deposits, north China craton (hebei province, China). *Chem. Geol.* 264, 101–121. doi:10.1016/j.chemgeo.2009.02.020

Cook, N. J., Ciobanu, C. L., Meria, D., Silcock, D., and Wade, B. (2013). Arsenopyrite-pyrite association in an orogenic gold ore: Tracing mineralization history from textures and trace elements. *Econ. Geol.* 108, 1273–1283. doi:10.2113/econgeo.108.6.1273

Deditius, A. P., Reich, M., Kesler, S. E., Utsunomiya, S., Chryssoulis, S. L., Walshe, J., et al. (2014). The coupled geochemistry of Au and as in pyrite from hydrothermal ore deposits. *Geochim. Cosmochim. Acta* 140, 644–670. doi:10.1016/j.gca.2014.05.045

Deng, J., Qiu, K. F., Wang, Q. F., Goldfarb, R., Yang, L. Q., Zi, J. W., et al. (2020a). *In situ* dating of hydrothermal monazite and implications on the geodynamic controls of ore formation in the Jiaodong gold province, eastern China. *Econ. Geol.* 115, 671–685. doi:10.5382/econgeo.4711

Deng, J., Liu, X. F., Wang, Q. F., and Pan, R. G. (2015a). Origin of the Jiaodong-type Xinli gold deposit, Jiaodong Peninsula, China: Constraints from fluid inclusion and C-D–O–S–Sr isotope compositions. *Ore Geol. Rev.* 65, 674–686. doi:10.1016/j.oregeorev.2014.04.018

Deng, J., Liu, X., Wang, Q., Dilek, Y., and Liang, Y. (2017). Isotopic characterization and petrogenetic modeling of early cretaceous mafic diking—lithospheric extension in the north China craton, eastern Asia. *GSA Bull.* 129, 1379–1407. doi:10.1130/b31609.1

Deng, J., Wang, C. M., Bagas, L., Carranza, E. J. M., and Lu, Y. (2015b). Cretaceous -Cenozoic tectonic history of the Jiaojia Fault and gold mineralization in the Jiaodong Peninsula, China: Constraints from zircon U-Pb: Illite K-Ar and apatite fission track thermochronometry. *Min. Depos.* 50 (8), 987–1006. doi:10.1007/s00126-015-0584-1

Deng, J., Wang, C. M., Bagas, L., Santosh, M., and Yao, E. Y. (2018). Crustal architecture and metallogenesis in the south-eastern North China Craton. *Earth. Sci. Rev.* 182, 251–272. doi:10.1016/j.earscirev.2018.05.001

Deng, J., and Wang, Q. F. (2016). Gold mineralization in China: Metallogenic provinces, deposit types and tectonic framework. *Gondwana Res.* 36, 219–274. doi:10.1016/j.gr.2015.10.003

Deng, J., Wang, Q., Santosh, M., Liu, X., and Yang, L. (2020c). Remobilization of metasomatized mantle lithosphere: A new model for the jiaodong gold province, eastern China. *Min. Depos.* 55, 257–274. doi:10.1007/s00126-019-00925-0

Deng, J., Yang, L. Q., Groves, D. I., Zhang, L., and Wang, Q. F. (2020b). An integrated mineral system model for the gold deposits of the giant Jiaodong province, eastern China. *Earth-Science Rev.* 208, 103274. doi:10.1016/j.earscirev.2020.103274

Deng, J., Yang, L. Q., and Wang, Q. F. (2006). Introduction to the composition and evolution of the gold metallogenic system in the Jiaodong ore concentration area. *Mineral. Deposits* 25 (S1), 67–70.

Fan, H. R., Feng, K., and Li, X. H. (2016). Jiaodong-korea peninsula mesozoic gold mineralization. *Acta Petrol. Sin.* 32 (10), 3225–3238.

Feng, K., Fan, H. R., Groves., David I., Yang, K. F., Liu, X., Cai, Y. C., et al. (2020). Geochronological and sulfur isotopic evidence for the Genesis of the post-magmatic, deeply sourced, and anomalously gold-rich Daliuhang orogenic deposit, Jiaodong, China. *Min. Depos.* 55, 293–308. doi:10.1007/s00126-019-00882-8

Feng, K., Fan, H. R., Hu, F. F., Yang, K. F., Liu, X., Shangguan, Y. N., et al. (2018). Involvement of anomalously As-Au-rich fluids in the mineralization of the Heilan'gou gold deposit, Jiaodong, China: Evidence from trace element mapping and *in-situ* sulfur isotope composition. *J. Asian Earth Sci.* 160, 304–321. doi:10.1016/j.jseaes.2017.12.023

Gammons, C. H., and Williams Jones, A. E. (1995). The solubility of Au-Ag alloy + AgCl in HCl/NaCl solutions at 300°C: New data on the stability of Au (1) chloride complexes in hydrothermal fluids. *Geochimica Cosmochimica Acta* 59 (17), 3453–3468. doi:10.1016/0016-7037(95)00234-q;

Goldfarb, R. J. M., and Santosh, M. (2014). The dilemma of the Jiaodong gold deposits: Are they unique? *Geosci. Front.* 5, 139–153. doi:10.1016/j.gsf.2013.11.001

Guo, L. N., Huang, C. M., and Zhang, L. (2019). Source of ore-forming fluids in the luoshan gold deposit, jiaodong: Constrains from REE and trace element features of auriferous pyrite in the altered-rock type and auriferous quartz vein type ores. *Geoscience* 33 (1), 121–136. doi:10.19657/j.geoscience.1000-8527.2019.01.12

Hayashi, K. I., and Ohmoto, H. (1991). Solubility of gold in NaCl- and H_2S-bearing aqueous solutions at 250–350 °C. *Geochim. Cosmochim. Acta* 55, 2111–2126. doi:10.1016/0016-7037(91)90091-i

Helgeson, H. C., and Garrels, R. M. (1968). Hydrothermal transport and deposition of gold. *Econ. Geol.* 63 (6), 622–635. doi:10.2113/gsecongeo.63.6.622

Henley, R. W. (1973). Solubility of gold in hydrothermal chloride solutions. *Solubility gold hydrothermal chloride solutionsChemical Geol.* 11 (2), 73–87. doi:10.1016/0009-2541(73)90044-2

Hou, M. L., Ding, X., and Jiang, S. Y. (2004). Lead and sulfur isotope geochemistry of the hexi gold deposit in Penglai, eastern Shandong. *Acta Geosci. Sin.* 25 (2), 145–150.

Hou, M. L., Jiang, S. Y., and Ling, H. F. (2006). S-Pb isotope geochemistry and Rb-Sr geochronology of the Penglai gold field in the eastern Shandong Province. *Acta Petrol. Sin.* 22 (10), 2525–2533.

Hou, M. L., Jiang, S. Y., Shen, K., Lian, G. J., Liu, Q. C., and Xiao, F. L. (2007a). Fluid inclusion and H-O isotope study of gold mineralization in the Penglai gold field, Eastern Shangdong. Acta Petrol. *Sin* 23, 2241–2256.

Hou, M. L., Jiang, Y. H., Jiang, S. Y., Ling, H. F., and Zhao, K. D. (2007b). Contrasting origins of late mesozoic adakitic granitoids from the northwestern jiaodong peninsula, east China: Implications for crustal thickening to delamination. *Geol. Mag.* 144, 619–631. doi:10.1017/s0016756807003494

Hu, H. L., Fan, H. R., Santosh, M., Liu, X., Cai, Y. C., and Yang, K. F. (2020). Ore-forming processes in the Wang'ershan gold deposit (Jiaodong, China): Insight from microtexture, mineral chemistry and sulfur isotope compositions. *Ore Geol. Rev.* 123, 103600. doi:10.1016/j.oregeorev.2020.103600

Huang, D. Y. (1994). Sulfur isotope studies of the metallogenic series of gold deposits in Jiaodong (East Shandong) area. *Mineral Deposits* 13, 75–87.

Ilchik, R. P., and Barton, M. D. (1997). An amagmatic origin of Carlin-type gold deposits. *Econ. Geol.* 92, 269–288.

Jiang, M. Y. (2019). Metallogeneses and Tectonic Setting Analysis of Shaling Gold Deposit in Jiaodong. *Diss. Subm. Hebei Geo Univ.*. Master Degree of Structural Geology, 1–60.

Kusebauch, C., Gleeson, S. A., and Oelze, M. (2019). Coupled partitioning of Au and as into pyrite controls formation of giant Au deposits. *Sci. Adv.* 5, eaav5891–8. doi:10.1126/sciadv.aav5891

Large, R. R., Danyushevsky, L., Hollit, C., Maslennikov, V., Meffre, S., Gilbert, S., et al. (2009). Gold and trace element zonation in Pyrite using a laser imaging technique: Implications for the timing of gold in orogenic and Carlin-Style sediment-hosted deposits. *Econ. Geol.* 104, 635–668. doi:10.2113/gsecongeo.104.5.635

Large, R. R., Halpin, J. A., Danyushevsky, L. V., Maslennikov, V. V., Bull, S. W., Long, J. A., et al. (2014). Trace element content of sedimentary pyrite as a new proxy for deep-time ocean–atmosphere evolution. *Earth Planet. Sci. Lett.* 389, 209–220. doi:10.1016/j.epsl.2013.12.020

Li, J., Song, M. C., Liang, J. L., MengYao, J., ShiYong, L., Zheng, D., et al. (2020a). Source of ore-forming fluids of the Jiaojia deeply-seated gold deposit: Evidences from trace elements and sulfur-helium-argon isotopes of pyrite. *Acta Petrol. Sin.* 36 (1), 297–313. doi:10.18654/1000-0569/2020.01.23

Li, L., Santosh, M., and Li, S. R. (2015). The 'jiaodong type' gold deposits: Characteristics, origin and prospecting. *Ore Geol. Rev.* 65, 589–611. doi:10.1016/j.oregeorev.2014.06.021

Li, R. H., Wang, X. Q., Yang, L. Q., Zhang, B. M., Liu, Q. Q., and Liu, D. S. (2020b). The characteristic of microstructural deformation of gold bearing pyrite in Jiaodong: The links between nanoscale gold enrichment and crystal distortion. *Ore Geol. Rev.* 122 495–504. doi:10.1016/j.oregeorev.2020.103495

Li, S. X., Liu, C. C., and An, Y. H. (2007). *Jiaodong gold mine geology*. Beijing: Geological Publishing House.

Liu, Y., Deng, J., and Wang, Z. L. (2014). Zircon U-Pb age, Lu-Hf isotopes and petrogeochemistry of the monzogranites from Xincheng gold deposit, northwestern Jiaodong Peninsula, China. *Acta Petrol. Sin.* 30 (9), 2559–2573.

Liu, Y. S., Hu, Z. C., Gao, S., Detlef, G., Xu, J., Gao, C. G., et al. (2008). *In situ* analysis of major and trace elements of anhydrous minerals by LA-ICP-MS without applying an internal standard. *Chem. Geol.* 257, 34–43. doi:10.1016/j.chemgeo.2008.08.004

Lu, H. Z., Fan, H. R., and Ni, P. (2004). *Fluid inclusions*. Beijing: Science Publishing House, 1–485.

Ma, W. D., Zhang, D. R., Wang, Z. L., Lu, A. H., Cui, Y., and Zuo, H. Y. (2015). A comparison study on mineralization characteristics in Dayingezhuang and Xiadian gold deposits, Eastern Shangdong Province. *Bull. Miner. Petrol* 34, 191–200.

Meng, L., Zhu, S. Y., Li, X. C., Chen, W. T., Xian, H. Y., Gao, X. Y., et al. (2022). Incorporation mechanism of structurally bound gold in pyrite: Insights from an integrated chemical and atomic-scale microstructural study. *Am. Mineralogist* 107, 603–613. doi:10.2138/am-2021-7812

Möller, P., and Kersten, G. (1994). Electrochemical accumulation of visible gold on pyrite and arsenopyrite surfaces. *Min. Depos.* 29, 404–413. doi:10.1007/bf01886958

Muntean, J. L., Cline, J. S., Simon, A. C., and Longo, A. A. (2011). Magmatic-hydrothermal origin of Nevada's Carlin-type gold deposits. *Nat. Geosci.* 4, 122–127. doi:10.1038/ngeo1064

Ogryzlo, S. P. (1935). Hydrothermal experiments with gold. *Econ. Geol.* 30 (4), 400–424. doi:10.2113/gsecongeo.30.4.400

Palenik, C. S., Utsunomiya, S., Reich, M., Kesler, S. E., Wang, L., and Ewing, R. C. (2004). Invisible" gold revealed: Direct imaging of gold nanoparticles in a Carlin-type deposit. *Am. Mineralogist* 89, 1359–1366. doi:10.2138/am-2004-1002

Peterson, E. C., and Mavrogenes, J. A. (2014). Linking high-grade gold mineralization to earthquake-induced fault-valve processes in the Porgera gold deposit, Papua New Guinea. *Geology* 42, 383–386. doi:10.1130/g35286.1

Ramboz, C., Pichavant, M., and Weisbrod, A. (1982). Fluid immiscibility in natural processes: Use and misuse of fluid inclusion data. *Chem. Geol.* 37 (1/2), 29–48. doi:10.1016/0009-2541(82)90065-1

Reich, M., Kesler, S. E., Utsunomiya, S., Palenik, C. S., Chryssoulis, S. L., and Ewing, R. (2005). Solubility ofgold in arsenianpyrite. *Geochim. Cosmochim. Acta* 69, 2781–2796. doi:10.1016/j.gca.2005.01.011

Renders, P. J., and Seward, T. M. (1989). The stability of hydrosulphido- and sulphido-complexes of Au(I) and Ag(I) at 25°C. *Geochim. Cosmochim. Acta* 53 (2), 245–253. doi:10.1016/0016-7037(89)90377-3

Roedder, E. (1984). "Fluid inclusions," in *Mineralogical society of America* (Chantilly: Mineralogical Society of America), 646.

Román, C. C., Yagüe, C., Arrillaga, J. A., Lothon, M., Pardyjak, E. R., Lohou, F., et al. (2019). Comparing mountain breezes and their impacts on CO_2 mixing ratios at three contrasting areas. *Atmos. Res.* 221, 111–126. doi:10.1016/j.atmosres.2019.01.019

Seward, T. M. (1991). The hydrothermal geochemistry of gold. *Gold Metallogeny Explor.* 42, 37–62. doi:10.1007/978-1-4613-0497-5_2

Shen, K., Shu, L., and Liu, P. R. (2018). Origin and significance of mica-bearing fluid inclusions in the altered wall rocks of wangjiazhuang copper-molybdenum deposit, zouping country, Shandong province. *Acta Petrol. Sin.* 34 (12), 3509–3524.

Shepherd, T. J., and Chenery, S. R. (1995). Laser ablation ICP-ms elemental analysis of individual fluid inclusions:an evaluation study. *Geochimica Cosmochimica Acta* 59 (19), 3997–4007. doi:10.1016/0016-7037(95)00294-a

Shu, L., Shen, K., Yang, R. C., Song, Y., Sun, Y., Shan, W., et al. (2020). SEM-CL study of quartz containing fluid inclusions in wangjiazhuang porphyry copper (-Molybdenum) deposit, western Shandong, China. *J. Earth Sci.* 31 (2), 330–341. doi:10.1007/s12583-019-1025-3

Simon, G., Huang, H., Penner-Hahn, J. E., Kesler, S. E., and Kao, L. S. (1999a). Oxidation state of gold and arsenic in gold-bearing arsenian pyrite. *Am. Mineralogist* 84, 1071–1079. doi:10.2138/am-1999-7-809

Simon, G., Kesler, S. E., and Chryssoulis, S. (1999b). Geochemistry and textures of gold-bearing arsenian pyrite, Twin Creeks, Nevada: Implications for deposition of gold in Carlin-type deposit. *Econ. Geol.* 94, 405–421. doi:10.2113/gsecongeo.94.3.405

Song, M. C., Li, S. Z., Santosh, M., Zhao, S., Yu, S., Yi, P. H., et al. (2015). Types, characteristics and metallogenesis of gold deposits in the jiaodong peninsula, eastern north China craton. *Ore Geol. Rev.* 65, 612–625. doi:10.1016/j.oregeorev.2014.06.019

Steele-MacInnis, M., Ridley, J., Lecumberri-Sanchez, P., Schlegel, T. U., and Heinrich, C. A. (2016). Application of low-temperature microthermometric data for interpreting multicomponent fluid inclusion compositions. *Earth-Science Rev.* 159, 14–35. doi:10.1016/j.earscirev.2016.04.011

Steele-MacInnis, M., Bodna, R. J., and Naden, J. (2011). Numerical model to determine the composition H_2O-NaCl-$CaCl_2$ fluid inclusions based on microthermometric and microanalytical data. *Geochimica Cosmochimica Acta* 75 (1), 21–40. doi:10.1016/j.gca.2010.10.002

Stefánsson, A., and Seward, T. M. (2004). Gold (I) complexing in aqueous sulphide solutions to 500°C at 500 bar. *Geochim. Cosmochim. Acta* 68, 4121–4143. doi:10.1016/j.gca.2004.04.006

Tanner, D., Henley, R. W., Mavrogenes, J. A., and Holden, P. (2016). Sulfur isotope and trace element systematics of zoned pyrite crystals from the El Indio Au-Cu-Ag deposit, Chile. *Contrib. Mineral. Pet.* 171, 33–17. doi:10.1007/s00410-016-1248-6

Tian, R. C., Li, D. P., Zhang, W., Tian, J. X., Yu, X. W., Geng, K. K., et al. (2022). The mixingof Mesozoic crust-mantle magma is the key to the source of large amounts of gold deposits in the Jiaobei uplift, China. *Acta Petrol. Sinica.* 38, 23–40. doi:10.18654/1000-0569/2022.01.03

Wang, Q. F., Lin, Q. W., Zhao, H. S., Groves, D. I., Weng, W. J., Xue, S. C., et al. (2021). Towards a universal model for orogenic gold systems: A perspective based on Chinese examples with geodynamic, temporal, and deposit-scale structural and geochemical diversity. *Earth-Science Rev.* 224, 103861. doi:10.1016/j.earscirev.2021.103861

Wang, Y. J., Shen, L. J., and Zhu, Y. Z. (2018). Characteristics of fluid inclusion of Houge'Zhuang gold deposit in Penglai area in Shandong province. *Shandong Land Resour.* 34 (3), 15–20.

Wang, Y. W., Zhu, F. S., and Gong, R. T. (2002). Tectonic isotope geochemistry further study on sulphur isotope of Jiaodong Gold Concentration Area. *Gold* 23, 1–16.

Wang, Z. L., Gong, Q. J., and Yang, L. Q. (2011). Timing of structural-thermal events in the Wang'ershan gold deposit, Eastern Shandong: Evidences from field investigations. *Geol. Explor.* 47 (6), 1067–1076.

Wang, Z. L., Yang, L. Q., Guo, L. N., Marsh, E., Liu, Y., Zhang, C., et al. (2015). Fluid immiscibility and gold deposition in the xincheng deposit, jiaodong peninsula, China: A fluid inclusion study. *Ore Geol. Rev.* 65, 701–717. doi:10.1016/j.oregeorev.2014.06.006

Wen, B. J., Fan, H. R., Hu, F. F., Liu, X., Yang, K. F., Sun, Z. F., et al. (2016). Fluid evolution and ore Genesis of the giant sanshandao gold deposit, jiaodong gold province, China: Constrains from geology, fluid inclusions and H-O-S-He-Ar isotopic compositions. *J. Geochem. Explor.* 171, 96–112. doi:10.1016/j.gexplo.2016.01.007

Wen, B. J., Fan, H. R., Santosh, M., Hu, F. F., Pirajno, F., and Yang, K. F. (2015). Genesis of two different types of gold mineralization in the Linglong gold field, China: Constrains from geology, fluid inclusions and stable isotope. *Ore Geol. Rev.* 65, 643–658. doi:10.1016/j.oregeorev.2014.03.018

Williams-Jones, A. E., Bowell, R. J., and Migdisov, A. A. (2009). Gold in solution. *Elements* 5, 281–287. doi:10.2113/gselements.5.5.281

Wood, S. A. (1989). Raman spectroscopic determination of the speciation of ore metals in hydrothermal solutions: I. Speciation of antimony in alkaline sulfide solutions at 25°C. *Geochimica Cosmochimica Acta* 53, 237–244. doi:10.1016/0016-7037(89)90376-1

Wu, Y. F., Evans, K., Li, J. W., Fougerouse, D., Large, R. R., and Guagliardo, P. (2019a). Metal remobilization and ore-fluid perturbation during episodic replacement of auriferous pyrite from an epizonal orogenic gold deposit. *Geochim. Cosmochim. Acta* 245, 98–117. doi:10.1016/j.gca.2018.10.031

Xing, Y. L., Brugger, J., Tomkins, A., and Shvarov, Y. R. (2019). Arsenic evolution as a tool for understanding formation of pyritic gold ores. *Geology* 47, 335–338. doi:10.1130/g45708.1

Yan, Y. T., Zhang, N., Li, S. R., and Li, Y. S. (2014). Mineral chemistry and isotope geochemistry of pyrite from the Heilangou gold deposit, Jiaodong Peninsula, Eastern China. *Geosci. Front.* 5, 205–213. doi:10.1016/j.gsf.2013.05.003

Yang, F., Santosh, M., Glorie, S., Jepson, G., Xue, F., and Kim, S. W. (2020). Meso-cenozoic multiple exhumation in the Shandong peninsula, eastern north China craton: Implications for lithospheric destruction. *Lithos* 370, 105597. doi:10.1016/j.lithos.2020.105597

Yang, F., Santosh, M., and Kim, S. W. (2018a). Mesozoic magmatism in the eastern North China Craton: Insights on tectonic cycles associated with progressive craton destruction. *Gondwana Res.* 60, 153–178. doi:10.1016/j.gr.2018.04.003

Yang, F., Santosh, M., and Tang, L. (2018b). Extensive crustal melting during craton destruction: Evidence from the mesozoic magmatic suite of junan, eastern north China craton. *J. Asian Earth Sci.* 157, 119–140. doi:10.1016/j.jseaes.2017.07.010

Yang, K. F., Jiang, P., Fan, H. R., Zuo, Y. B., and Yang, Y. H. (2018). Tectonic transition from a compressional to extensional metallogenic environment at ~120 Ma revealed in the Hushan gold deposit, Jiaodong, North China Craton. *J. Asian Earth Sci.* 160, 408–425. doi:10.1016/j.jseaes.2017.08.014

Yang, L. Q., Deng, J., Guo, R. P., Guo, L., Wang, Z., Chen, B., et al. (2016a). World-class Xincheng gold deposit: An example from the giant Jiaodong gold province. *Geosci. Front.* 7 (3), 419–430. doi:10.1016/j.gsf.2015.08.006

Yang, L. Q., Deng, J., Wang, Z. L., Guo, L. N., Li, R. H., Groves, D. I., et al. (2016b). Relationships between gold and pyrite at the Xincheng gold deposit, Jiaodong Peninsula, China: Implications for gold source and deposition in a brittle epizonal environment. *Econ. Geol.* 111, 105–126. doi:10.2113/econgeo.111.1.105

Yang, L. Q., Deng, J., Wang, Z. L., Zhang, L., Guo, L. N., Song, M. C., et al. (2014). Mesozoic gold metallogenic system of the Jiaodong gold province, eastern China. *Acta Petrol. Sin.* 30 (9), 2447–2467.

Zhai, M. G., and Santosh, M. (2011). The early precambrian odyssey of the north China craton: A synoptic overview. *Gondwana Res.* 20 (1), 6–25. doi:10.1016/j.gr.2011.02.005

Zhang, J., Deng, J., Chen, H. Y., Yang, L. Q., Cooke, D., Danyushevsky, L., et al. (2014). LA-ICP-MS trace element analysis of pyrite from the Chang'an gold deposit, Sanjiang region, China: Implication for ore-forming process. *Gondwana Res.* 26, 557–575. doi:10.1016/j.gr.2013.11.003

Zhang, L., Weinberg, R. F., Yang, L. Q., Groves, D. I., Deng, J., Matchan, E., et al. (2020). Mesozoic orogenic gold mineralization in the jiaodong peninsula, China: A focused event at 120±2 Ma during cooling of pregold granite intrusions:. *Econ. Geol.* 115, 415–441. doi:10.5382/econgeo.4716

Zhang, Z., Mandal, A. K., Wang, N., Keck, C. L., Zimonjic, D. B., Popescu, N. C., et al. (1999). Palmitoyl-protein thioesterase gene expression in the developing mouse brain and retina: Implications for early loss of vision in infantile neuronal ceroid lipofuscinosis.Super large gold deposit exploration perspective in jiaolai basin of jiaodong gold metallogenetic domain. *Gene* 28, 203–211. doi:10.1016/s0378-1119(99)00050-5

Zhu, R. X., Fan, H. R., Li, J. W., Meng, Q. R., Li, S. R., and Zeng, Q. D. (2015). Decratonic gold deposits. *Sci. China Earth Sci.* 58, 1523–1537. doi:10.1007/s11430-015-5139-x

Zotov, A. V., Baranova, N. N., and Bannykh, L. N. (1996). Solubility of the gold sulfides Au 2S and AuAgS in solutions containing hydrogen sulfide at 25 ~ 80°C and pressures of 1 and 500 bar. *Geochem. Int.* 34 (3), 216–221.